

Hemodynamic Deconvolution Demystified: Sparsity-Driven Regularization at Work

Eneko Uruñuela^{a,b,*}, Thomas A.W. Bolton^{c,d}, Dimitri Van De Ville^{c,e}, César Caballero-Gaudes^{a,*}

^a*Basque Center on Cognition, Brain and Language (BCBL), Donostia-San Sebastián, Spain.*

^b*University of the Basque Country (EHU/UPV), Donostia-San Sebastián, Spain.*

^c*Ecole Polytechnique Fédérale de Lausanne (EPFL), Lausanne, Switzerland.*

^d*Gamma Knife Center, Department of Clinical Neuroscience, Centre Hospitalier Universitaire Vaudois (CHUV), Lausanne, Switzerland*

^e*Faculty of Medicine, University of Geneva, Geneva, Switzerland*

Abstract

Deconvolution of the hemodynamic response is an important step to access short timescales of brain activity recorded by functional magnetic resonance imaging (fMRI). Albeit conventional deconvolution algorithms have been around for a long time (e.g., Wiener deconvolution), recent state-of-the-art methods based on sparsity-pursuing regularization are attracting increasing interest to investigate brain dynamics and connectivity with fMRI. This technical note revisits the main concepts underlying two main methods, Paradigm Free Mapping and Total Activation, in the most accessible way. Despite their apparent differences in the formulation, these methods are theoretically equivalent as they represent the synthesis and analysis sides of the same problem, respectively. We demonstrate this equivalence in practice with their best-available implementations using both simulations, with different signal-to-noise ratios, and experimental fMRI data acquired during a motor task and resting-state. We evaluate the parameter settings that lead to equivalent results, and showcase the potential of these algorithms compared to other common approaches. This note is useful for practitioners interested in gaining a better understanding of state-of-the-art hemodynamic deconvolution, and aims to answer questions that practitioners often have regarding the differences between the two methods.

Keywords: fMRI deconvolution, paradigm free mapping, total activation, temporal regularization

1. Introduction

Functional magnetic resonance imaging (fMRI) data analysis is often directed to identify and disentangle the neural processes that occur in different brain regions during task or at rest. As the blood oxygenation level-dependent (BOLD) signal of fMRI is only a proxy for neuronal activity mediated through neurovascular coupling, an intermediate step that estimates the activity-inducing signal, at the timescale of fMRI, from the BOLD timeseries can be useful. Conventional analysis of task fMRI data relies on the general linear models (GLM) to establish statistical parametric maps of brain activity by regression of the empirical timecourses against hypothetical ones built from

*Corresponding authors

Email addresses: e.urunuela@bcbl.eu (Eneko Uruñuela), c.caballero@bcbl.eu (César Caballero-Gaudes)

9 the knowledge of the experimental paradigm. However, timing information of the paradigm can be
10 unknown, inaccurate, or insufficient in some scenarios such as naturalistic stimuli, resting-state, or
11 clinically-relevant assessments.

12 Deconvolution and methods alike are aiming to estimate neuronal activity by undoing the
13 blurring effect of the hemodynamic response, characterized as a hemodynamic response function
14 (HRF)¹. Given the inherently ill-posed nature of hemodynamic deconvolution, due to the strong
15 temporal low-pass characteristics of the HRF, the key is to introduce additional constraints in
16 the estimation problem that are typically expressed as regularizers. For instance, the so-called
17 Wiener deconvolution is expressing a “minimal energy” constraint on the deconvolved signal, and
18 has been used in the framework of psychophysiological interaction analysis to compute the interac-
19 tion between a seed’s activity-inducing timecourse and an experimental modulation (Glover, 1999;
20 Gitelman et al., 2003; Gerchen et al., 2014; Di and Biswal, 2018; Freitas et al., 2020). Complement-
21 arily, the interest in deconvolution has increased to explore time-varying activity in resting-state
22 fMRI data (Prete et al., 2017; Keilholz et al., 2017; Lurie et al., 2020; Bolton et al., 2020). In that
23 case, the aim is to gain better insights of the neural signals that drive functional connectivity at
24 short time scales, as well as learning about the spatio-temporal structure of functional components
25 that dynamically construct resting-state networks and their interactions (Karahanoglu and Ville,
26 2017).

27 Deconvolution of the resting-state fMRI signal has illustrated the significance of transient, sparse
28 spontaneous events (Petridou et al., 2012; Allan et al., 2015) that refine the hierarchical clusteriza-
29 tion of functional networks (Karahanoglu et al., 2013) and reveal their temporal overlap based
30 on their signal innovations not only in the human brain (Karahanoglu and Ville, 2015), but also
31 in the spinal cord (Kinany et al., 2020). Similar to task-related studies, deconvolution allows to
32 investigate modulatory interactions within and between resting-state functional networks (Di and
33 Biswal, 2013, 2015). In addition, decoding of the deconvolved spontaneous events allows to decipher
34 the flow of spontaneous thoughts and actions across different cognitive and sensory domains while
35 at rest (Karahanoglu and Ville, 2015; Gonzalez-Castillo et al., 2019; Tan et al., 2017). Beyond find-
36 ings on healthy subjects, deconvolution techniques have also proven its utility in clinical conditions
37 to characterize functional alterations of patients with a progressive stage of multiple sclerosis at
38 rest (Bommarito et al., 2020), to find functional signatures of prodromal psychotic symptoms and
39 anxiety at rest on patients suffering from schizophrenia (Zöller et al., 2019), to detect the foci of
40 interictal events in epilepsy patients without an EEG recording (Lopes et al., 2012; Karahanoglu
41 et al., 2013), or to study functional dissociations observed during non-rapid eye movement sleep
42 that are associated with reduced consolidation of information and impaired consciousness (Tarun
43 et al., 2020).

44 The algorithms for hemodynamic deconvolution can be classified based on the assumed hemo-
45 dynamic model and the optimization problem used to estimate the neuronal-related signal. Most
46 approaches assume a linear time-invariant model for the hemodynamic response that is inverted
47 by means of variational (regularized) least squares estimators (Glover, 1999; Gitelman et al., 2003;
48 Gaudes et al., 2010, 2012, 2013; Caballero-Gaudes et al., 2019; Hernandez-Garcia and Ulfarsson,
49 2011; Karahanoglu et al., 2013; Cherkaooui et al., 2019; Costantini et al., 2021; Hütel et al., 2021),
50 logistic functions (Bush and Cisler, 2013; Bush et al., 2015; Loula et al., 2018), probabilistic mixture

¹Note that the term deconvolution is also alternatively employed to refer to the estimation of the hemodynamic response shape assuming a known activity-inducing signal or neuronal activity (Goutte et al., 2000; Marrelec et al., 2002; Ciuciu et al., 2003; Casanova et al., 2008).

models (Pidnebesna et al., 2019), convolutional autoencoders (Hütel et al., 2018) or nonparametric homomorphic filtering (Sreenivasan et al., 2015). Alternatively, several methods have also been proposed to invert non-linear models of the neuronal and hemodynamic coupling (Riera et al., 2004; Penny et al., 2005; Friston et al., 2008; Havlicek et al., 2011; Aslan et al., 2016; Madi and Karameh, 2017; Ruiz-Euler et al., 2018).

Among the variety of approaches, those based on regularized least squares estimators have been employed more often due to their appropriate performance at small spatial scales (e.g., voxelwise). Relevant for this work, two different formulations can be established for the regularized least-squares deconvolution problem, either based on a synthesis- or analysis-based model (Elad et al., 2007; Ortelli and van de Geer, 2019). The rationale of the synthesis-based model is that we know or suspect that the true signal (here, the neuronally-driven BOLD component of the fMRI signal) can be represented as a linear combination of predefined patterns or dictionary atoms (for instance, the hemodynamic response function). In contrast, the analysis-based approach considers that the true signal is analyzed by some relevant operator and the resulting signal is small (i.e., sparse).

As members of the groups that developed Paradigm Free Mapping (synthesis-based solved with regularized least-squares estimators such as ridge-regression Gaudes et al. 2010 or LASSO Gaudes et al. 2013) and Total Activation (analysis-based also solved with a regularized least-squares estimator using generalized total variation Karahanoglu et al. 2011; Karahanoglu et al. 2013) deconvolution methods for fMRI data analysis, we are often contacted by researchers who want to know about the similarities and differences between the two methods and which one is better. It depends—and to clarify this point, this note revisits synthesis- and analysis-based deconvolution methods for fMRI data and comprises four sections. First, we present the theory behind these two deconvolution approaches based on regularized least squares estimators that promote sparsity: Paradigm Free Mapping (PFM) (Gaudes et al., 2013) — available in AFNI as *3dPFM*² and *3dMEPFM*³ for single-echo and multi-echo data, respectively — and Total Activation (TA) (Karahanoglu et al., 2013) — available as part of the *iCAPs toolbox*⁴. We describe the similarities and differences in their analytical formulations, and how they can be related to each other. Next, we assess their performance controlling for a fair comparison on simulated and experimental data. Finally, we discuss their benefits and shortcomings and conclude with our vision on potential extensions and developments.

2. Theory

2.1. Notations and definitions

Matrices of size N rows and M columns are denoted by boldface capital letters, e.g., $\mathbf{X} \in \mathbb{R}^{N \times M}$, whereas column vectors of length N are denoted as boldface lowercase letters, e.g., $\mathbf{x} \in \mathbb{R}^N$. Scalars are denoted by lowercase letters, e.g., k . Continuous functions are denoted by brackets, e.g., $h(t)$, while discrete functions are denoted by square brackets, e.g., $x[k]$. The Euclidean norm of a matrix \mathbf{X} is denoted as $\|\mathbf{X}\|_2$, the ℓ_1 -norm is denoted by $\|\mathbf{X}\|_1$ and the Frobenius norm is denoted by $\|\mathbf{X}\|_F$. The discrete integration (\mathbf{L}) and difference (\mathbf{D}) operators are defined as:

²https://afni.nimh.nih.gov/pub/dist/doc/program_help/3dPFM.html

³https://afni.nimh.nih.gov/pub/dist/doc/program_help/3dMEPFM.html

⁴<https://c4science.ch/source/iCAPs/>

$$\mathbf{L} = \begin{bmatrix} 1 & 0 & \dots & & \\ 1 & 1 & 0 & \dots & \\ 1 & 1 & 1 & 0 & \dots \\ \vdots & \ddots & \ddots & \ddots & \ddots \end{bmatrix}, \quad \mathbf{D} = \begin{bmatrix} 1 & 0 & \dots & & \\ 1 & -1 & 0 & \dots & \\ 0 & \ddots & \ddots & \ddots & \dots \\ \vdots & \ddots & 0 & 1 & -1 \end{bmatrix}.$$

89 *2.2. Conventional general linear model analysis*

Conventional general linear model (GLM) analysis puts forward a number of regressors incorporating the knowledge about the paradigm or behavior. For instance, the timing of epochs for a certain condition can be modeled as an indicator function $p(t)$ (e.g., Dirac functions for event-related designs or box-car functions for block-designs) convolved with the hemodynamic response function (HRF) $h(t)$, and sampled at TR resolution (Friston et al., 1994, 1998; Boynton et al., 1996; Cohen, 1997):

$$x(t) = p * h(t) \rightarrow x[k] = p * h(k \cdot \text{TR}).$$

The vector $\mathbf{x} = [x[k]]_{k=1,\dots,N} \in \mathbb{R}^N$ then constitutes the regressor modelling the hypothetical response, and several of them can be stacked as columns of the design matrix $\mathbf{X} = [\mathbf{x}_1 \dots \mathbf{x}_L] \in \mathbb{R}^{N \times L}$, leading to the well-known GLM formulation:

$$\mathbf{y} = \mathbf{X}\boldsymbol{\beta} + \mathbf{e}, \quad (1)$$

90 where the empirical timecourse $\mathbf{y} \in \mathbb{R}^N$ is explained by a linear combination of the regressors in \mathbf{X}
 91 weighted by the parameters in $\boldsymbol{\beta} \in \mathbb{R}^L$ and corrupted by additive noise $\mathbf{e} \in \mathbb{R}^N$. Under independent
 92 and identically distributed Gaussian assumptions of the latter, the maximum likelihood estimate of
 93 the parameter weights reverts to the ordinary least-squares estimator; i.e., minimizing the residual
 94 sum of squares between the fitted model and measurements. The number of regressors L is typically
 95 much less than the number of measurements N , and thus the regression problem is over-determined
 96 and does not require additional constraints or assumptions (Henson and Friston, 2007).

In the deconvolution approach, no prior knowledge of the hypothetical response is taken into account, and the purpose is to estimate the deconvolved activity-inducing signal \mathbf{s} from the measurements \mathbf{y} , which can be formulated as the signal model

$$\mathbf{y} = \mathbf{H}\mathbf{s} + \mathbf{e}, \quad (2)$$

where $\mathbf{H} \in \mathbb{R}^{N \times N}$ is a Toeplitz matrix that represents the discrete convolution with the HRF, and $\mathbf{s} \in \mathbb{R}^N$ is a length- N vector with the unknown activity-inducing signal. Note that the temporal resolution of the activity-inducing signal and the corresponding Toeplitz matrix is generally assumed to be equal to the TR of the acquisition, but it could also be higher if an upsampled estimate is desired. Despite the apparent similarity with the GLM equation, there are two important differences. First, the multiplication with the design matrix of the GLM is an expansion as a weighted linear combination of its columns, while the multiplication with the HRF matrix represents a convolution operator. Second, determining \mathbf{s} is an ill-posed problem given the nature of the HRF. As it can be seen intuitively, the convolution matrix \mathbf{H} is highly collinear (i.e., its columns are highly correlated) due to large overlap between shifted HRFs (see Figure 2C), thus introducing uncertainty in the estimates of \mathbf{s} when noise is present. Consequently, additional assumptions under the form of

regularization terms (or priors) in the estimate are needed to reduce their variance. In the least squares sense, the optimization problem to solve is given by

$$\hat{\mathbf{s}} = \arg \min_{\mathbf{s}} \frac{1}{2} \|\mathbf{y} - \mathbf{H}\mathbf{s}\|_2^2 + \Omega(\mathbf{s}). \quad (3)$$

The first term quantifies data fitness, which can be justified as the log-likelihood term derived from Gaussian noise assumptions, while the second term $\Omega(\mathbf{s})$ brings in regularization and can be interpreted as a prior on the activity-inducing signal. For example, the ℓ_2 -norm of \mathbf{s} (i.e., $\Omega(\mathbf{s}) = \lambda \|\mathbf{s}\|_2^2$) is imposed for ridge regression or Wiener deconvolution, which introduces a trade-off between the data fit term and “energy” of the estimates that is controlled by the regularization parameter λ . regularized terms are related to the elastic net (i.e., $\Omega(\mathbf{x}) = \lambda_1 \|\mathbf{x}\|_2^2 + \lambda_2 \|\mathbf{x}\|_1$) [REF].

2.3. Paradigm Free Mapping

In paradigm free mapping (PFM), the formulation of Eq. (3) was considered equivalently as fitting the measurements using the atoms of the HRF dictionary (i.e., columns of \mathbf{H}) with corresponding weights (entries of \mathbf{s}). This model corresponds to a synthesis formulation. In Gaudes et al. 2013 a sparsity-pursuing regularization term was introduced on \mathbf{s} , which in a strict way reverts to choosing $\Omega(\mathbf{s}) = \lambda \|\mathbf{s}\|_0$ as the regularization term and solving the optimization problem (Bruckstein et al., 2009). However, finding the optimal solution to the problem demands an exhaustive search across all possible combinations of the columns of \mathbf{H} . Hence, a pragmatic solution is to solve the convex-relaxed optimization problem for the ℓ_1 -norm, commonly known as Basis Pursuit Denoising (Chen et al., 2001) or equivalently as the least absolute shrinkage and selection operator (LASSO) (Tibshirani, 1996):

$$\hat{\mathbf{s}} = \arg \min_{\mathbf{s}} \frac{1}{2} \|\mathbf{y} - \mathbf{H}\mathbf{s}\|_2^2 + \lambda \|\mathbf{s}\|_1, \quad (4)$$

which provides fast convergence to a global solution. Imposing sparsity on the activity-inducing signal implies that it is assumed to be well represented by a reduced subset of few non-zero coefficients at the fMRI timescale, which in turn trigger event-related BOLD responses. Hereinafter, we refer to this assumption as the *spike model*. [However, even if PFM was developed as a spike model, its formulation in Eq.\(4\) can be extended to estimate the innovation signal, i.e., the derivative of the activity-inducing signal, as shown in section 2.5.](#)

2.4. Total Activation

Alternatively, deconvolution can be formulated as if the signal to be recovered directly fits the measurements and at the same time satisfies some suitable regularization, which leads to

$$\hat{\mathbf{x}} = \arg \min_{\mathbf{x}} \frac{1}{2} \|\mathbf{y} - \mathbf{x}\|_2^2 + \Omega(\mathbf{x}). \quad (5)$$

Under this analysis formulation, total variation (TV), i.e., the ℓ_1 -norm of the derivative $\Omega(\mathbf{x}) = \lambda \|\mathbf{D}\mathbf{x}\|_1$, is a powerful regularizer since it favors recovery of piecewise-constant signals (Chambolle, 2004). Going beyond, the approach of generalized TV introduces an additional differential operator $\mathbf{D}_{\mathbf{H}}$ in the regularizer that can be tailored as the inverse operator of a linear system (Karahanoglu et al., 2011), that is, $\Omega(\mathbf{x}) = \lambda \|\mathbf{D}\mathbf{D}_{\mathbf{H}}\mathbf{x}\|_1$. In the context of hemodynamic deconvolution, Total Activation is proposed for which the discrete operator $\mathbf{D}_{\mathbf{H}}$ is derived from the inverse of the continuous-domain linearized Balloon-Windkessel model (Buxton et al., 1998; Friston et al., 2000).

¹¹⁸ The interested reader is referred to (Khalidov et al., 2011; Karahanoglu et al., 2011; Karahanoglu
¹¹⁹ et al., 2013) for a detailed description of this derivation.

Therefore, the solution of the Total Activation (TA) problem

$$\hat{\mathbf{x}} = \arg \min_{\mathbf{x}} \frac{1}{2} \|\mathbf{y} - \mathbf{x}\|_2^2 + \lambda \|\mathbf{D}\mathbf{D}_{\mathbf{H}}\mathbf{x}\|_1 \quad (6)$$

¹²⁰ will yield the activity-related signal \mathbf{x} for which the activity-inducing signal $\mathbf{s} = \mathbf{D}_{\mathbf{H}}\mathbf{x}$ and the
¹²¹ so-called innovation signal $\mathbf{u} = \mathbf{D}\mathbf{s}$, i.e., the derivate of the activity-inducing signal, will also be
¹²² available, as they are required for the regularization. We refer to modeling the activity-inducing
¹²³ signal based on the innovation signal as the *block model*. Nevertheless, even if TA was originally
¹²⁴ developed as a block model, its formulation in Eq.(6) can be made equivalent to the spike model
¹²⁵ as shown in section 2.5.

¹²⁶ 2.5. Unifying both perspectives

¹²⁷ PFM and TA are based on the synthesis- and analysis-based formulation of the deconvolution
¹²⁸ problem, respectively. They are also tailored for the spike and block model, respectively. In the first
¹²⁹ case, the recovered deconvolved signal is synthesized to be matched to the measurements, while in
¹³⁰ the second case, the recovered signal is directly matched to the measurements but needs to satisfy
¹³¹ its analysis in terms of deconvolution. This also corresponds to using the forward or backward
¹³² model of the hemodynamic system, respectively. Hence, it is possible to make both approaches
¹³³ equivalent (Elad et al., 2007)⁵.

¹³⁴ To start with, TA can be made equivalent to PFM by adapting it for the spike model; i.e., when
¹³⁵ removing the derivative operator \mathbf{D} of the regularizer in Eq. (6), it can be readily verified that
¹³⁶ replacing in that case $\mathbf{x} = \mathbf{H}\mathbf{s}$ leads to identical equations and thus both assume a spike model,
¹³⁷ since \mathbf{H} and $\mathbf{D}_{\mathbf{H}}$ will cancel out each other (Karahanoglu et al., 2011)⁶.

Conversely, the PFM spike model can also accommodate the TA block model by modifying Eq.
(4) with the forward model $\mathbf{y} = \mathbf{H}\mathbf{L}\mathbf{u} + \mathbf{e}$. Here, the activity-inducing signal \mathbf{s} is rewritten in terms
of the innovation signal \mathbf{u} as $\mathbf{s} = \mathbf{L}\mathbf{u}$ where the matrix \mathbf{L} is the first-order integration operator
(Cherkaoui et al., 2019; Uruñuela et al., 2020). This way, PFM can estimate the innovation signal
 \mathbf{u} as follows:

$$\hat{\mathbf{u}} = \arg \min_{\mathbf{u}} \frac{1}{2} \|\mathbf{y} - \mathbf{H}\mathbf{L}\mathbf{u}\|_2^2 + \lambda \|\mathbf{u}\|_1, \quad (7)$$

¹³⁸ and becomes equivalent to TA by replacing $\mathbf{u} = \mathbf{D}\mathbf{D}_{\mathbf{H}}\mathbf{x}$, and thus adopting the block model. Based
¹³⁹ on the previous equations (4), (6) and (7), it is clear that both PFM and TA can operate under the
¹⁴⁰ spike and block models, providing a convenient signal model according to the different assumptions
¹⁴¹ of the underlying neuronal-related signal. This work evaluates the core of the two techniques; i.e.,
¹⁴² the regularized least-squares problem with temporal regularization without considering the spatial
¹⁴³ regularization term originally incorporated in TA. For the remainder of this paper, we will use the
¹⁴⁴ PFM and TA formalisms with both spike and block models.

⁵Without dwelling into technicalities, for total variation, this equivalence is correct up to the constant, which is in the null space of the derivative operator.

⁶Again, this holds up to elements of the null space.

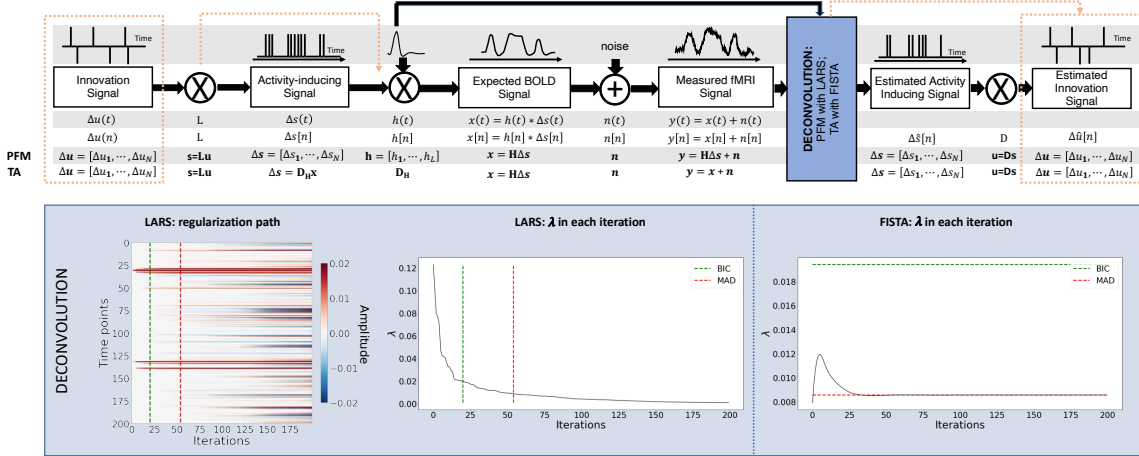


Figure 1: Flowchart detailing the different steps of the fMRI signal and the deconvolution methods described. The orange arrows indicate the flow to estimate the innovation signals, i.e., the derivative of the activity-inducing signal. The blue box depicts the iterative *modus operandi* of the two algorithms used in this paper to solve the paradigm free mapping (PFM) and total activation (TA) deconvolution problems. The plot on the left shows the regularization path obtained with the least angle regression (LARS) algorithm, where the x-axis illustrates the different iterations of the algorithm, the y-axis represents points in time, and the color describes the amplitude of the estimated signal. The middle plot depicts the decreasing values of λ for each iteration of LARS as the regularization path is computed. The green and red dashed lines in both plots illustrate the Bayesian information criterion (BIC) and median absolute deviation (MAD) solutions, respectively. Comparatively, the changes in λ when the fast iterative shrinkage-thresholding algorithm (FISTA) method is made to converge to the MAD estimate of the noise are shown on the right. Likewise, the λ corresponding to the BIC and MAD solutions are shown with dashed lines.

145 2.6. Algorithms and parameter selection

146 Despite their apparent resemblance, the practical implementations of the PFM and TA meth-
 147 ods proposed different algorithms to solve the corresponding optimization problem and select an
 148 adequate regularization parameter λ (Gaudes et al., 2013; Karahanoglu et al., 2013). The PFM
 149 implementation available in AFNI employs the least angle regression (LARS) (Efron et al., 2004),
 150 whereas the TA implementation uses the fast iterative shrinkage-thresholding algorithm (FISTA)
 151 (Beck and Teboulle, 2009). The blue box in Figure 1 provides a descriptive view of the iterative
 152 *modus operandi* of the two algorithms.

153 On the one hand, LARS is a homotopy approach that computes all the possible solutions to
 154 the optimization problem and their corresponding value of λ ; i.e., the regularization path, and
 155 the solution according to the Bayesian Information Criterion (BIC) (Schwarz, 1978), was recom-
 156 mended as the most appropriate in the case of PFM approaches since AIC often tends to overfit
 157 the signal(Gaudes et al., 2013; Caballero-Gaudes et al., 2019).

On the other hand, FISTA is an extension of the classical gradient algorithm that provides fast convergence for large-scale problems. In the case of FISTA though, the regularization parameter λ must be selected prior to solving the problem, but can be updated in every iteration so that the residuals of the data fit converge to an estimated noise level of the data $\hat{\sigma}$:

$$\lambda^{n+1} = \frac{N\hat{\sigma}}{\frac{1}{2}\|\mathbf{y} - \mathbf{x}^n\|_F^2} \lambda^n, \quad (8)$$

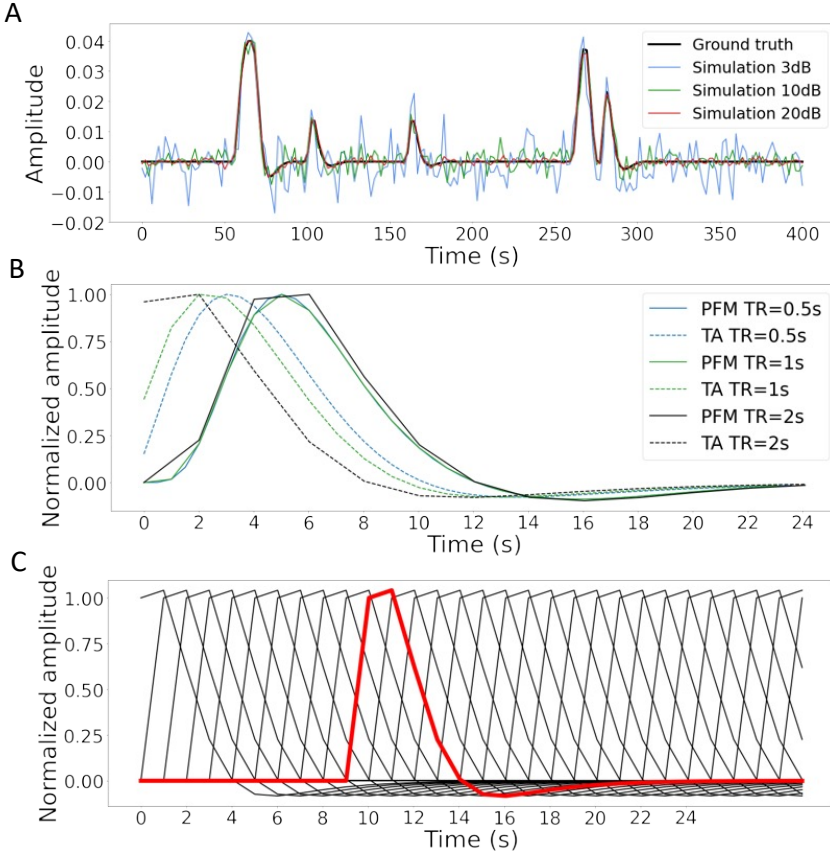


Figure 2: A) Simulated signal with different SNRs (20 dB, 10 dB and 3 dB) and ground truth given in signal percentage change (SPC). B) Canonical HRF models typically used by PFM (solid line) and TA (dashed line) at TR = 0.5 s (blue), TR = 1 s (green) and TR = 2 s (black). Without loss of generality, the waveforms are scaled to unit amplitude for visualization. C) Representation of shifted HRFs at TR = 2 s that build the design matrix for PFM when the HRF model has been matched to that in TA. The red line corresponds to one of the columns of the HRF matrix.

158 where x^n is the n^{th} iteration estimate, λ^n and λ^{n+1} are the n^{th} and $n + 1^{th}$ iteration values for the
 159 regularization parameter λ , and N is the number of points in the time-course. The pre-estimated
 160 noise level can be obtained as the median absolute deviation (MAD) of the fine-scale wavelet
 161 coefficients (Daubechies, order 3) of the fMRI timecourse. The MAD criterion has been adopted
 162 in TA (Karahanoglu et al., 2013). Of note, similar formulations based on the MAD estimate have
 163 also been applied in PFM formulations (Gaudes et al., 2012, 2011).

164 **3. Methods**

165 *3.1. Simulated data*

In order to compare the two methods while controlling for their correct performance, we created a simulation scenario that can be found in the GitHub repository shared in Section 6. For the sake of illustration, we describe here the simulations corresponding to a timecourse with a duration of 400 seconds (TR = 2 s) where the activity-inducing signal includes 5 events, which are convolved with the canonical HRF. Different noise sources (physiological, thermal, and motion-related) were also added and we simulated three different scenarios with varying signal-to-noise ratios (SNR = [20 dB, 10 dB, 3 dB]) that represent high, medium and low contrast-to-noise ratios as shown in Figure 2A. Noise was created following the procedure in (Gaudes et al., 2013) as the sum of uncorrelated Gaussian noise and sinusoidal signals to simulate a realistic noise model with thermal noise, cardiac and respiratory physiological fluctuations, respectively. The physiological signals were generated as

$$\sum_{i=1}^2 \frac{1}{2^{i-1}} (\sin(2\pi f_{r,i}t + \phi_{r,i}) + \sin(2\pi f_{c,i}t + \phi_{c,i})), \quad (9)$$

166 with up to second-order harmonics per cardiac ($f_{c,i}$) and respiratory ($f_{r,i}$) component that were
167 randomly generated following normal distributions with variance 0.04 and mean if_r and if_c , for
168 $i = [1, 2]$. We set the fundamental frequencies to $f_r = 0.3$ Hz for the respiratory component (Birn
169 et al., 2006)) and $f_c = 1.1$ Hz for the cardiac component (Shmueli et al., 2007)). The phases of
170 each harmonic ϕ were randomly selected from a uniform distribution between 0 and 2π radians.
171 To simulate physiological noise that is proportional to the change in BOLD signal, a variable ratio
172 between the physiological (σ_P) and the thermal (σ_0) noise was modeled as $\sigma_P/\sigma_0 = a(tSNR)^b + c$,
173 where $a = 5.01 \times 10^{-6}$, $b = 2.81$, and $c = 0.397$, following the experimental measures available in
174 Table 3 from (Triantafyllou et al., 2005)).

175 *3.2. Experimental data*

176 To compare the performance of the two approaches as well as illustrate their operation, we
177 employ two representative experimental datasets.

178 **Motor task dataset:** One healthy subject was scanned in a 3T MR scanner (Siemens) under a
179 Basque Center on Cognition, Brain and Language Review Board-approved protocol. T2*-weighted
180 multi-echo fMRI data was acquired with a simultaneous-multislice multi-echo gradient echo-planar
181 imaging sequence, kindly provided by the Center of Magnetic Resonance Research (University of
182 Minnesota, USA) (Feinberg et al., 2010; Moeller et al., 2010; Setsompop et al., 2011), with the
183 following parameters: 340 scans, 52 slices, Partial-Fourier = 6/8, voxel size = $2.4 \times 2.4 \times 3$ mm 3 ,
184 TR = 1.5 s, TEs = 10.6/28.69/46.78/64.87/82.96 ms, flip angle = 70°, multiband factor = 4,
185 GRAPPA = 2.

186 During the fMRI acquisition, the subject performed a motor task consisting of five different
187 movements (left-hand finger tapping, right-hand finger tapping, moving the left toes, moving the
188 right toes and moving the tongue) that were visually cued through a mirror located on the head
189 coil. These conditions were randomly intermixed every 16 seconds, and were only repeated once
190 the entire set of stimuli were presented. Data preprocessing consisted of first, discarding the first 10
191 volumes of the functional data to achieve a steady state of magnetization. Then, image realignment
192 to the skull-stripped single-band reference image (SBRef) was computed on the first echo, and the
193 estimated rigid-body spatial transformation was applied to all other echoes (Jenkinson et al., 2012;
194 Jenkinson and Smith, 2001). A brain mask obtained from the SBRef volume was applied to all the
195 echoes and the different echo timeseries were optimally combined (OC) voxelwise by weighting each

timeseries contribution by its T2* value (Posse et al., 1999). AFNI (Cox, 1996) was employed for a detrending of up to 4th-order Legendre polynomials, within-brain spatial smoothing (3 mm FWHM) and voxelwise signal normalization to percentage change. Finally, distortion field correction was performed on the OC volume with Topup (Andersson et al., 2003), using the pair of spin-echo EPI images with reversed phase encoding acquired before the ME-EPI acquisition (Glasser et al., 2016).

Resting-state datasets: One healthy subject was scanned in a 3T MR scanner (Siemens) under a Basque Center on Cognition, Brain and Language Review Board-approved protocol. Two runs of T2*-weighted fMRI data were acquired during resting-state, each with 10 min duration, with 1) a standard gradient-echo echo-planar imaging sequence (monoband) (TR = 2000 ms, TE = 29 ms, flip-angle = 78°, matrix size = 64 × 64, voxel size = 3 × 3 × 3 mm³, 33 axial slices with interleaved acquisition, slice gap = 0.6 mm) and 2) a simultaneous-multislice gradient-echo echo-planar imaging sequence (multiband factor = 3, TR = 800 ms, TE = 29 ms, flip-angle = 60°, matrix size = 64 × 64, voxel size = 3 × 3 × 3 mm³, 42 axial slices with interleaved acquisition, no slice gap). Single-band reference images were also collected in both resting-state acquisitions for head motion realignment. Field maps were also obtained to correct for field distortions.

During both acquisitions, participants were instructed to keep their eyes open, fixating a white cross that they saw through a mirror located on the head coil, and not to think about anything specific. The data was pre-processed using AFNI (Cox, 1996). First, volumes corresponding to the initial 10 seconds were removed to allow for a steady-state magnetization. Then, the voxel time-series were despiked to reduce large-amplitude deviations and slice-time corrected. Inhomogeneities caused by magnetic susceptibility were corrected with FUGUE (FSL) using the field map images (Jenkinson et al., 2012). Next, functional images were realigned to a base volume (monoband: volume with the lowest head motion; multiband: single-band reference image). Finally, a simultaneous nuisance regression step was performed comprising up to 6th-order Legendre polynomials, low-pass filtering with a cutoff frequency of 0.25 Hz (only on multiband data to match the frequency content of the monoband), 6 realignment parameters plus temporal derivatives, 5 principal components of white matter (WM), 5 principal components of lateral ventricle voxels (anatomical CompCor) (Behzadi et al., 2007) and 5 principal components of the brain's edge voxels ,(Patriat et al., 2015). WM, CSF and brain's edge-voxel masks were obtained from Freesurfer tissue and brain segmentations. In addition, scans with potential artifacts were identified and censored when the euclidean norm of the temporal derivative of the realignment parameters (ENORM) was larger than 0.4, and the proportion of voxels adjusted in the despiking step exceeded 10%.

3.3. Selection of the hemodynamic response function

In their original formulations, PFM and TA specify the discrete-time HRF in different ways. For PFM, the continuous-domain specification of the canonical double-gamma HRF (Henson and Friston, 2007) is sampled at the TR and then put as shifted impulse responses to build the matrix \mathbf{H} . In the case of TA, however, the continuous-domain linearized version of the balloon-windkessel model is discretized to build the linear differential operator in $\mathbf{D}_\mathbf{H}$. While the TR only changes the resolution of the HRF shape for PFM, the impact of an equivalent impulse response of the discretized differential operator at different TR is more pronounced. As shown in Figure 2B, longer TR leads to equivalent impulse responses of TA that are shifted in time, provoking a lack of the initial baseline and rise of the response. We refer the reader to Figure S1 to see the differences in the estimation of the activity-inducing and innovation signals when both methods use the HRF in their original formulation. To avoid differences between PFM and TA based on their built-in

240 HRF, we choose to build the synthesis operator \mathbf{H} with shifted versions of the HRF given by the
241 TA analysis operator (e.g., see Figure 2C for the TR=2s case).

242 *3.4. Selection of the regularization parameter*

243 We use the simulated data to compare the performance of the two deconvolution algorithms
244 with both BIC and MAD criteria to set the regularization parameter λ (see section 2.6). We also
245 evaluate if the algorithms behave differently in terms of the estimation of the activity-inducing
246 signal $\hat{\mathbf{s}}$ using the spike model described in (4) and the block model based on the innovation signal
247 $\hat{\mathbf{u}}$ in (7).

248 For selection based on the BIC, LARS was initially performed with the PFM deconvolution
249 model to obtain the solution for every possible λ in the regularization path. Then, the values of λ
250 corresponding to the BIC optimum were adopted to solve the TA deconvolution model by means
251 of FISTA.

252 For a selection based on the MAD estimate of the noise, we apply the temporal regularization in
253 its original form for TA, whereas for PFM the selected λ corresponds to the solution whose residuals
254 have the closest standard deviation to the estimated noise level of the data $\hat{\sigma}$.

255 *3.5. Analyses in experimental fMRI data*

Difference between approaches: To assess the discrepancies between both approaches when applied on experimental fMRI data, we calculate the square root of the sum of squares of the differences (RSSD) between the activity-inducing signals estimated with PFM and TA on the three experimental datasets as

$$\text{RSSD} = \sqrt{\frac{1}{N} \sum_{k=1}^N (\hat{s}_{\text{PFM}}[k] - \hat{s}_{\text{TA}}[k])^2}, \quad (10)$$

256 where N is the number of timepoints of the acquisition. The RSSD of the innovation signals $\hat{\mathbf{u}}$ was
257 computed equally.

258 **Task fMRI data:** In the analysis of the motor task data, we evaluate the performance of PFM
259 and TA in comparison with a conventional General Linear Model analysis (*3dDeconvolve* in AFNI)
260 that takes advantage of the information about the duration and onsets of the motor trials. Given
261 the block design of the motor task, we only make this comparison with the block model.

262 **Resting-state fMRI data:** We also illustrate the usefulness of deconvolution approaches in
263 the analysis of resting-state data where information about the timings of neuronal-related BOLD
264 activity cannot be predicted. Apart from being able to explore individual maps of deconvolved
265 activity (i.e., innovation signals, activity-inducing signals, or hemodynamic signals) at the temporal
266 resolution of the acquisition (or deconvolution), here we calculate the [average extreme points of the](#)
267 [activity-inducing and innovation maps \(given that these examples do not have a sufficient number](#)
268 [of scans to perform a clustering step\)](#) and illustrate how popular approaches like co-activation
269 patterns (CAPs)(Tagliazucchi et al., 2012; Liu et al., 2018) and innovation-driven co-activation
270 patterns (iCAPs) (Karahanoglu and Ville, 2015) can be applied on the deconvolved signals to reveal
271 patterns of coordinated brain activity. To achieve this, we calculate the average time-series in a seed
272 of 9 voxels located in the precuneus, supramarginal gyrus, and occipital gyri independently, and
273 solve the deconvolution problem to find the activity-inducing and innovation signals in the seeds.
274 We then apply a 95th percentile threshold and average the maps of the time-frames that survive the
275 threshold. Finally, we apply the same procedure to the original— i.e., non-deconvolved— signal in
276 the seed and compare the results with the widely-used seed correlation approach.

277 **4. Results**

278 *4.1. Performance based on the regularization parameter*

279 Figure 3A shows the regularization paths of PFM and TA side by side obtained for the spike
280 model of Eq. (4) for SNR=3 dB. The solutions for all three SNR conditions are shown in Figures S2
281 and S3. Starting from the maximum λ corresponding to a null estimate and for decreasing values
282 of λ , LARS computes a new estimate at the value of λ that reduces the sparsity promoted by the
283 l_1 -norm and causes a change in the active set of non-zero coefficients of the estimate (i.e., a zero
284 coefficient becomes non-zero or vice versa) as shown in the horizontal axis of the heatmaps. Vertical
285 dashed lines depict the selection of the regularization parameter based on the BIC, and thus, the
286 colored coefficients indicated by these depict the estimated activity-inducing signal \hat{s} . Figure 3B
287 illustrates the resulting estimates of the activity-inducing and activity-related hemodynamic signals
288 when basing the selection of λ on the BIC for SNR=3 dB. Given that the regularization paths of
289 both approaches are identical, it can be clearly observed that the BIC-based estimates are identical
290 too for the corresponding λ . Thus, Figures 3A, 3B, S2 and S3 demonstrate that, regardless of
291 the simulated SNR condition, the spike model of both deconvolution algorithms produces identical
292 regularization paths when the same HRF and regularization parameters are applied, and hence,
293 identical estimates of the activity-inducing signal \hat{s} and neuronal-related hemodynamic signal \hat{x} .
294 Likewise, Figure 3C demonstrates that the regularization paths for the block model defined in
295 Eqs. (6) and (7) also yield virtually identical estimates of the innovation signals for both PFM and
296 TA methods. Again, the BIC-based selection of λ is identical for both PFM and TA. As illustrated
297 in Figure 3D, the estimates of the innovation signal u also show no distinguishable differences
298 between the algorithms. Figures 3 A-D demonstrate that both PFM and TA yield equivalent
299 regularization paths and estimates of the innovation signal and activity-inducing signal regardless
300 of the simulated SNR condition when applying the same HRF and regularization parameters with
301 the block and spike models.

302 As for selecting λ with the MAD criterion defined in Eq. (8), Figure 3E depicts the estimated
303 activity-inducing and activity-related signals for the simulated low-SNR setting using the spike
304 model, while Figure 3F shows the estimated signals corresponding to the block model. Both plots
305 in Figure 3E and F depict nearly identical results between PFM and TA with both models. Given
306 that the regularization paths of both techniques are identical, minor dissimilarities are owing to the
307 slight differences in the selection of λ due to the quantization of the values returned by LARS.

308 *4.2. Performance on experimental data*

309 Figure 4 depicts the RSSD maps revealing differences between PFM and TA estimates for
310 the spike (Figure 4A and C) and block (Figure 4B and D) models when applied to the three
311 experimental fMRI datasets. The RSSD values are virtually negligible (i.e., depicted in yellow)
312 in most of the within-brain voxels and lower than the amplitude of the estimates of the activity-
313 inducing and innovation signals. Based on the maximum value of the range shown in each image,
314 we observe that the similarity between both approaches is more evident for the spike model (with
315 both selection criteria) and the block model with the BIC selection. However, given the different
316 approaches used for the selection of the regularization parameter λ based on the MAD estimate
317 of the noise (i.e., converging so that the residuals of FISTA are equal to the MAD estimate of the
318 noise for TA vs. finding the LARS residual that is closest to the MAD estimate of the noise),
319 higher RSSD values can be observed with the largest differences occurring in gray matter voxels.
320 These areas also correspond to low values of λ (see Figure S4) and MAD estimates of the noise

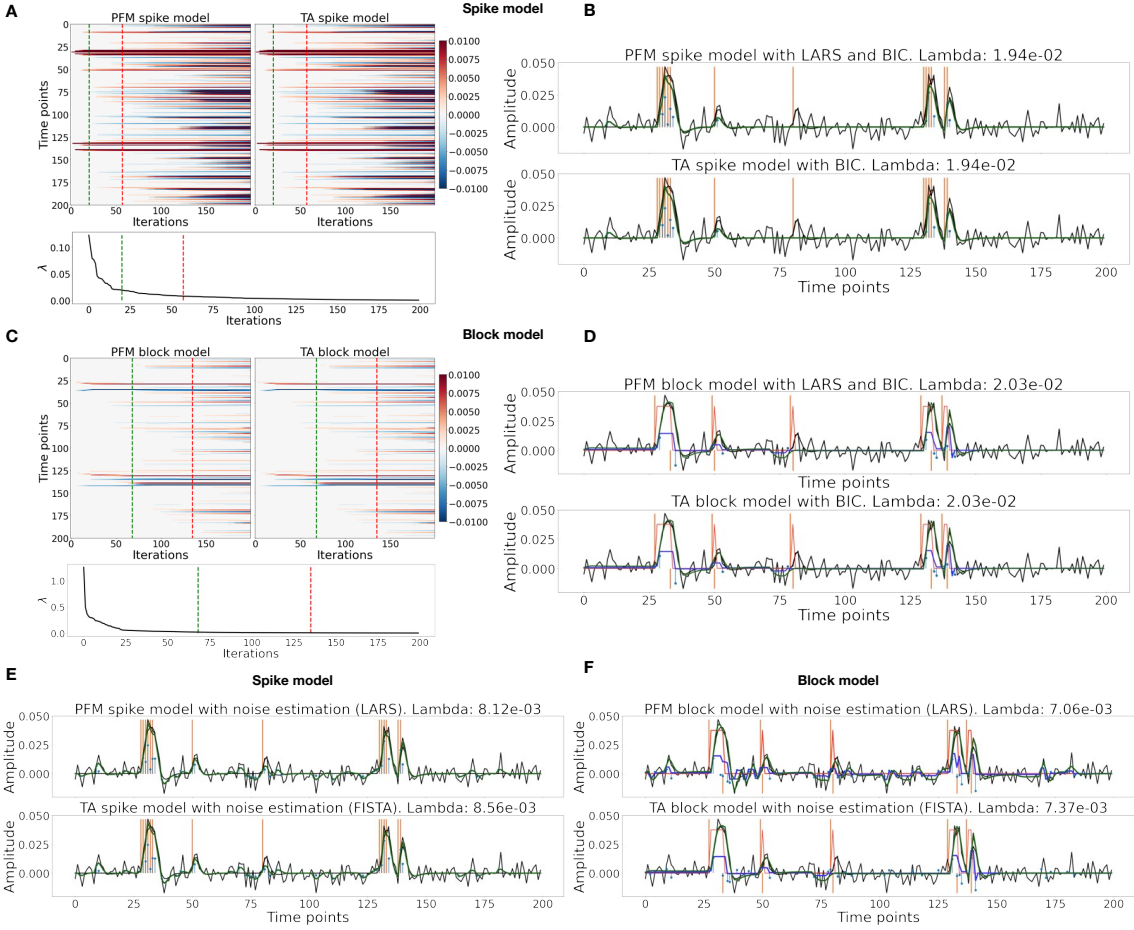


Figure 3: (A) Heatmap of the regularization paths of the activity-inducing signals (spike model) estimated with PFM and TA as a function of λ for the simulated data with SNR = 3 dB (x-axis: increasing number of iterations or λ as given by LARS; y-axis: time; color: amplitude). Vertical lines denote iterations corresponding to the BIC (dashed line) and MAD (dotted line) selection of λ . (B) Estimated activity-inducing (blue) and activity-related (green) signals with a selection of λ based on the BIC. Orange and red lines depict the ground truth. (C) Heatmap of the regularization paths of the innovation signals (block model) estimated with PFM and TA as a function of λ for the simulated data with SNR = 3 dB. (D) Estimated innovation (blue), activity-inducing (darker blue), and activity-related (green) signals with a selection of λ based on the BIC. (E) Activity-inducing and activity-related (fit, \times) signals estimated with PFM (top) and TA (bottom) when λ is selected based on the MAD method with the spike model, and (F) with the block model for the simulated data with SNR = 3 dB.

(see Figure S5), while the highest values are visible in regions with signal dropouts, ventricles, and white matter. These differences that arise from the differing methods to find the optimal regularization parameter based on the MAD estimate of the noise can be clearly seen in the root sum of squares (RSS) of the estimates of the two methods (Figure S6). These differences are also observable in the ATS calculated from estimates obtained with the MAD selection as shown in

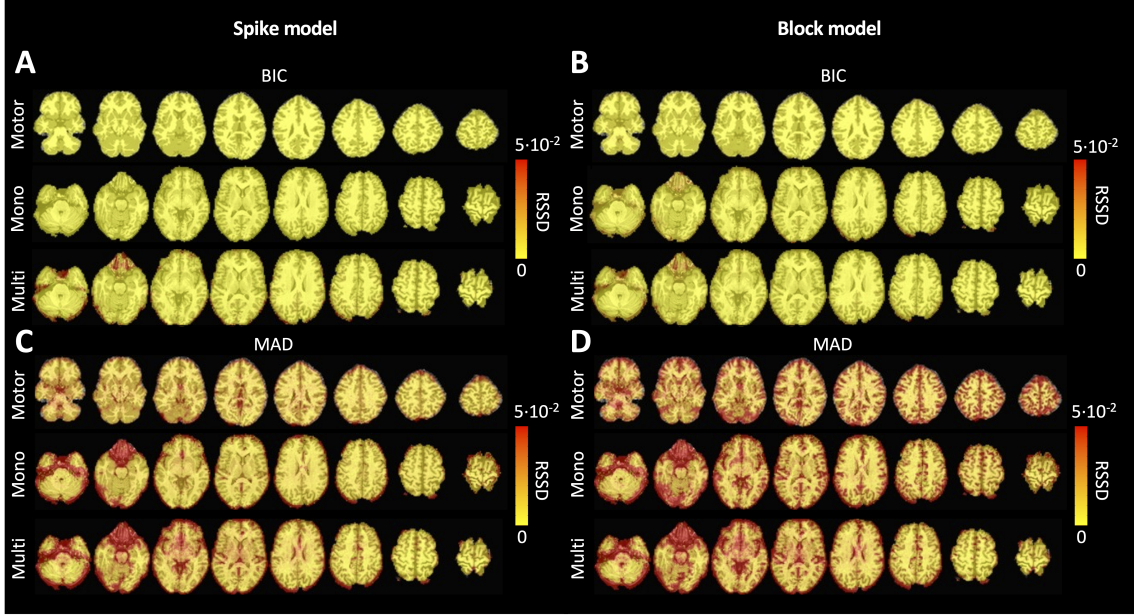


Figure 4: Square root of the sum of squared differences (RSSD) between the estimates obtained with PFM and TA for (A) spike model (activity-inducing signal) and BIC selection of λ , (B) block model (innovation signal) and BIC selection, (C) spike model (activity-inducing signal) and MAD selection, (D) block model (innovation signal) and MAD selection. RSSD maps are shown for the three experimental fMRI datasets: the motor task (Motor), the monoband resting-state (Mono), and the multiband resting-state (Multi) datasets.

326 Figure S9. However, the identical regularization paths shown in Figure S7 demonstrate that both
 327 methods perform equivalently on experimental data (see estimates of innovation signal obtained
 328 with an identical selection of λ in Figure S8). Hence, the higher RSSD values originate from the
 329 different methods to find the optimal regularization parameter based on the MAD estimate of the
 330 noise that yield different solutions as shown by the dashed vertical lines in Figure S7.

331 Figure 5 depicts the results of the analysis of the Motor dataset with the PFM and TA algorithms
 332 using the BIC selection of λ (see Figure S9 for results with MAD selection), as well as a conventional
 333 GLM approach. The Activation Time Series (top left), calculated as the sum of squares of all voxel
 334 amplitudes (positive vs. negative) for a given moment in time, obtained with PFM and TA show
 335 nearly identical patterns. These ATS help to summarize the four dimensional information available
 336 in the results across the spatial domain and identify instances of significant BOLD activity. The
 337 second to sixth rows show the voxel timeseries and the corresponding activity-related, activity-
 338 inducing and innovation signals obtained with PFM using the BIC criterion of representative voxels
 339 in the regions activated in each of the motor tasks. The TA-estimated time-series are not shown
 340 because they were virtually identical. The maps shown on the right correspond to statistical
 341 parametric maps obtained with the GLM for each motor condition ($p < 0.001$) as well as the maps
 342 of the PFM and TA estimates at the onsets of individual motor events (indicated with arrows in
 343 the timecourses). The estimated activity-related, activity-inducing and innovation signals clearly
 344 reveal the activity patterns of each condition in the task, as they exhibit a BOLD response locked to

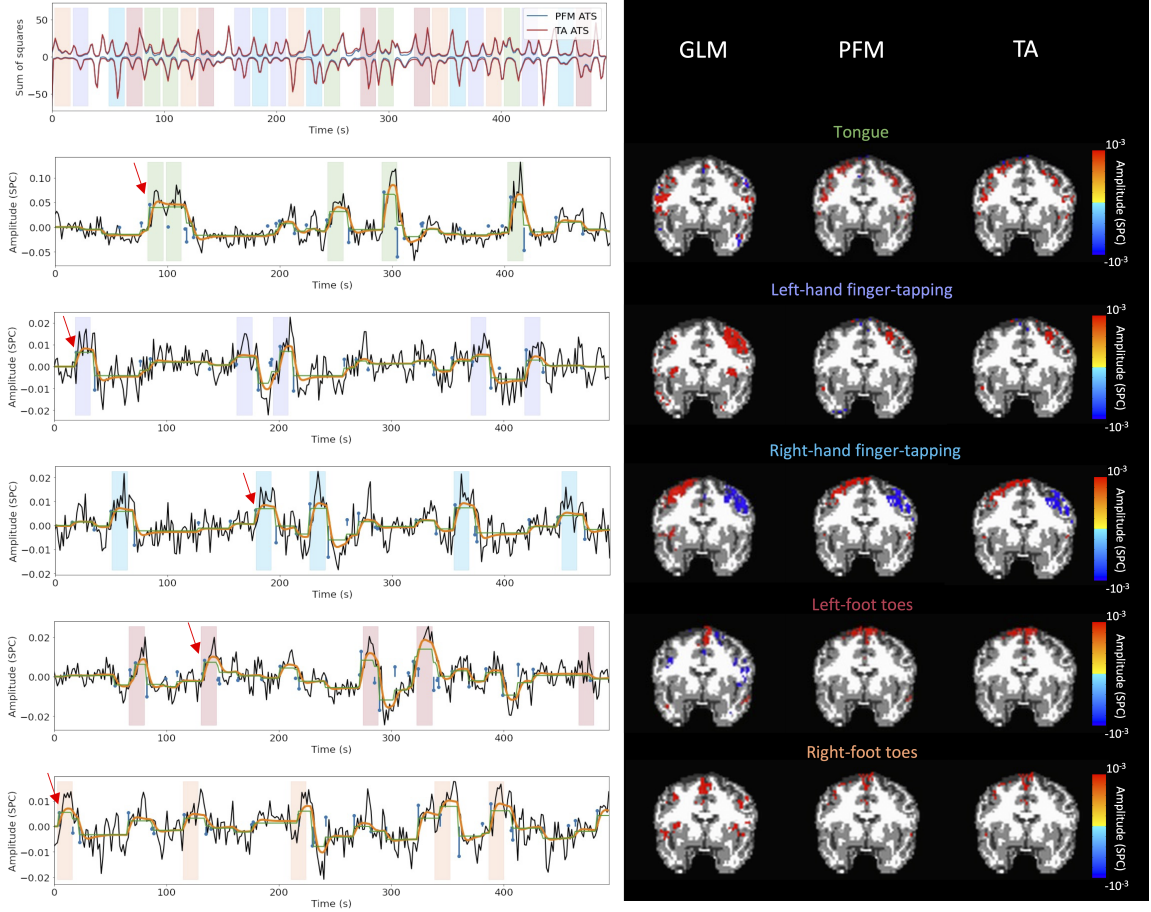


Figure 5: Activity maps of the motor task using a selection of λ based on the BIC estimate. Row 1: Activation time-series (ATS) of the innovation signals estimated by PFM (in blue) or TA (in red) calculated as the sum of squares of all voxels at every timepoint. Positive-valued and negative-valued contributions were separated into two distinct time-courses. Color-bands indicate the onset and duration of each condition in the task (green: tongue motion, purple: left-hand finger-tapping, blue: right-hand finger-tapping, red: left-foot toes motion, orange: right-foot toes motion). Rows 2-6: time-series of a representative voxel for each task with the PFM-estimated innovation (blue), PFM-estimated activity-inducing (green), and activity-related (i.e., fitted, orange) signals, with their corresponding GLM, PFM, and TA maps on the right (representative voxels indicated with green arrows). Amplitudes are given in signal percentage change (SPC). The maps shown on the right are sampled at the time-points labeled with the red arrows and display the innovation signals at these moments across the whole brain.

345 the onset and duration of the conditions. Overall, activity maps of the innovation signal obtained
 346 with PFM and TA highly resemble those obtained with a GLM for individual events, **with small**
 347 **differences arising from the distinct specificity of the GLM and deconvolution analyses**. Notice that
 348 the differences observed with the different approaches to select λ based on the MAD estimate shown
 349 in Figure 4 are reflected on the ATS shown in Figure S9 as well.

350 As an illustration of the insights that deconvolution methods can provide in the analysis of

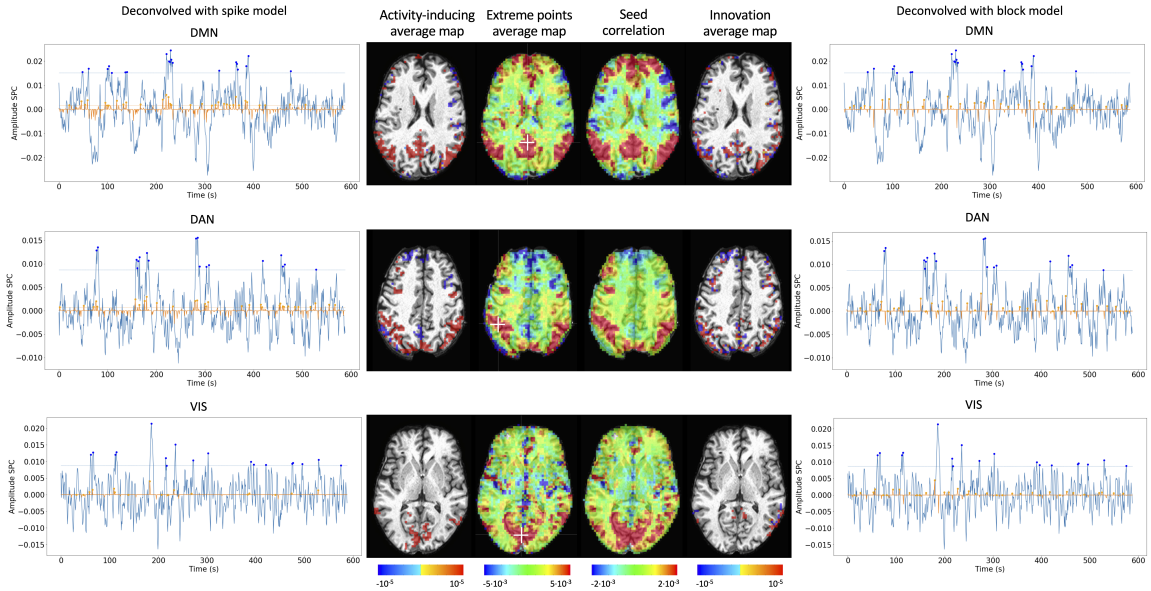


Figure 6: Average activity-inducing (left) and innovation (right) maps obtained from PFM-estimated activity-inducing and innovation signals, respectively, using a BIC-based selection of λ . Time-points selected with a 95th percentile threshold (horizontal lines) are shown over the average time-series (blue) in the seed region (white cross) and the deconvolved signals, i.e., activity inducing (left) and innovation (right) signals (orange). Average maps of extreme points and seed correlation maps are illustrated in the center.

resting-state data, Figure 6 depicts the average activity-inducing and innovation maps of common resting-state networks obtained from thresholding and averaging the activity-inducing and innovation signals, respectively, estimated from the resting-state multiband data using PFM with a selection of λ based on the BIC. The average activity-inducing maps obtained via deconvolution show spatial patterns of the default mode network (DMN), dorsal attention network (DAN), and visual network (VIS) that highly resemble the maps obtained with conventional seed correlation analysis using Pearson's correlation, and the average maps of extreme points of the signal (i.e., with no deconvolution). With deconvolution, the average activity-inducing maps seem to depict more accurate spatial delineation (i.e., less smoothness) than those obtained from the original data, while maintaining the structure of the networks. The BIC-informed selection of λ yields spatial patterns of average activity-inducing and innovation maps that are more sparse than those obtained with a selection of λ based on the MAD estimate (see Figure S10). Furthermore, the spatial patterns of the average innovation maps based on the innovation signals using the block model yield complementary information to those obtained with the activity-inducing signal since iCAPs allow to reveal regions with synchronous innovations, i.e., with the same upregulating and downregulating events. For instance, it is interesting to observe that the structure of the visual network nearly disappears in its corresponding average innovation maps, suggesting the existence of different temporal neuronal patterns across voxels in the primary and secondary visual cortices.

369 **5. Discussion**

370 Hemodynamic deconvolution can be formulated using a synthesis- and analysis-based approach
371 as proposed by PFM and TA, respectively. This work demonstrates that the theoretical equivalence
372 of **both approaches** is confirmed in practice given virtually identical results when the same HRF
373 model and equivalent regularization parameters are employed. Hence, we argue that previously ob-
374 served differences in performance can be explained by specific settings, such as the HRF model and
375 selection of the regularization parameter ([as shown in Figures 4,S6 and S7](#)), convergence thresh-
376 olds, as well as the addition of a spatial regularization term in the spatiotemporal TA formulation
377 ([Karahanoğlu et al., 2013](#)). [For instance, the use of PFM with the spike model in \(Tan et al., 2017\)](#)
378 was seen not to be ideal due to the prolonged trials in the paradigm, which better fit the block
379 model as described here ([7](#)). Similarly, all the works using the iCAPs approach, and thus the TA
380 implementation for deconvolution ([Kinany et al., 2020; Zöller et al., 2019; Pirondini et al., 2022](#)),
381 could alternatively use the PFM approach with the block model adding a spatial regularization
382 term, which would [yield identical results providing the same criterion is used to select the regular-](#)
383 [ization parameters](#). However, given the equivalence of the temporal deconvolution, incorporating
384 extra spatial or temporal regularization terms in the optimization problem should not modify this
385 equivalence providing convex operators are employed. For a convex optimization problem, with
386 a unique global solution, iterative shrinkage thresholding procedures alternating between the dif-
387 ferent regularization terms guarantee convergence; e.g., the generalized forward-backward splitting
388 ([Raguet et al., 2013](#)) algorithm originally employed for TA. Our findings are also in line with the
389 equivalence of analysis and synthesis methods in under-determined cases ($N \leq V$) demonstrated in
390 ([Elad et al., 2007](#)) and ([Ortelli and van de Geer, 2019](#)). [Using a lower regularization parameter \(i.e.,](#)
391 [penalty on the amplitude of the estimates\) makes the estimates more similar to the least-squares](#)
392 [solution, which results in higher sensitivity in detecting events. Conversely, employing a higher](#)
393 [λ leads to higher specificity at the cost of a decrease in sensitivity.](#) Still, we have shown that a
394 slight difference in the selection of the regularization parameter can lead to small differences in the
395 estimated signals when employing the block model with the MAD selection of λ . However, since
396 their regularization paths are equivalent, the algorithms can easily be forced to converge to the
397 same selection of λ , thus resulting in identical estimated signals.

398 Nevertheless, the different formulations of analysis and synthesis deconvolution models bring
399 along different kinds of flexibility. One notable advantage of PFM is that it can readily incorporate
400 any HRF as part of the synthesis operator ([Elad et al., 2007](#)), only requiring the sampled HRF at the
401 desired temporal resolution, which is typically equal to the TR of the acquisition. Conversely, TA
402 relies upon the specification of the discrete differential operator that inverts the HRF, which needs
403 to be derived either by the inverse solution of the sampled HRF impulse response, or by discretizing
404 a continuous-domain differential operator motivated by a biophysical model. The more versatile
405 structure of PFM allows for instance an elegant extension of the algorithm to multi-echo fMRI
406 data ([Caballero-Gaudes et al., 2019](#)) where multiple measurements relate to a common underlying
407 signal. Therefore, the one-to-many synthesis scenario (i.e., from activity-inducing to several activity-
408 related signals) is more cumbersome to express using TA; i.e., a set of differential operators should
409 be defined and the differences between their outputs constrained. Conversely, the one-to-many
410 analysis scenario (i.e., from the measurements to several regularizing signals) is more convenient
411 to be expressed by TA; e.g., combining spike and block regularizers. While the specification of the
412 differential operator in TA only indirectly controls the HRF, the use of the derivative operator to
413 enforce the block model, instead of the integrator in PFM, impacts positively the stability and rate
414 of the convergence of the optimization algorithms. Moreover, analysis formulations can be more

415 suitable for online applications that are still to be explored in fMRI data, but are employed for
416 calcium imaging deconvolution (Friedrich et al., 2017; Jewell et al., 2019), and which have been
417 applied for offline calcium deconvolution (Farouj et al., 2020).

418 Deconvolution techniques can be used before more downstream analysis of brain activity in terms
419 of functional network organization as they estimate interactions between voxels or brain regions that
420 occur at the activity-inducing level, and are thus less affected by the slowness of the hemodynamic
421 response compared to when the BOLD signals are analyzed directly. In addition, deconvolution
422 approaches hold a close parallelism to recent methodologies aiming to understand the dynamics of
423 neuronal activations and interactions at short temporal resolution and that focus on extreme events
424 of the fMRI signal (Lindquist et al., 2007). As an illustration, Figure 6 shows that the innovation-
425 or activity-inducing CAPs computed from deconvolved events in a single resting-state fMRI dataset
426 closely resemble the conventional CAPs computed directly from extreme events of the fMRI signal
427 (Liu and Duyn, 2013; Liu et al., 2013, 2018; Cifre et al., 2020a,b; Zhang et al., 2020; Tagliazucchi
428 et al., 2011, 2012, 2016; Rolls et al., 2021). Similarly, we hypothesize that these extreme events
429 will also show a close resemblance to intrinsic ignition events (Deco and Kringelbach, 2017; Deco
430 et al., 2017). As shown in the maps, deconvolution approaches can offer a more straightforward
431 interpretability of the activation events and resulting functional connectivity patterns. Here, CAPs
432 were computed as the average of spatial maps corresponding to the events of a single dataset.
433 Beyond simple averaging, clustering algorithms (e.g., K-means and consensus clustering) can be
434 employed to discern multiple CAPs or iCAPs at the whole-brain level for a large number of subjects.
435 Previous findings based on iCAPs have for instance revealed organizational principles of brain
436 function during rest (Karahanoglu and Ville, 2015) and sleep (Tarun et al., 2021) in healthy controls,
437 next to alterations in 22q11ds (Zoeller et al., 2019) and multiple sclerosis (Bommarito et al., in
438 press). Next to CAPs-inspired approaches, dynamic functional connectivity has recently been
439 investigated with the use of co-fluctuations and edge-centric techniques (Faskowitz et al., 2020;
440 Esfahlani et al., 2020; Jo et al., 2021; Sporns et al., 2021; van Oort et al., 2018). The activation
441 time series shown in Figure 5 aim to provide equivalent information to the root of sum of squares
442 timecourses used in edge-centric approaches, where timecourses with peaks delineate instances
443 of significant brain activity. Future work could address which type of information is redundant
444 or distinct across these frameworks. In summary, these examples illustrate that deconvolution
445 techniques can be employed prior to other computational approaches and could serve as an effective
446 way of denoising the fMRI data. We foresee an increase in the number of studies that take advantage
447 of the potential benefits of using deconvolution methods prior to functional connectivity analyses.

448 In sum, hemodynamic deconvolution approaches using sparsity-driven regularization are valuable
449 tools to complete the fMRI processing pipeline. Although the two approaches examined in
450 detail here provide alternative representations of the BOLD signals in terms of innovation and
451 activity-inducing signals, their current implementations have certain limitations, calling for further
452 developments or more elaborate models, where some of them have been initially addressed in the
453 literature. One relevant focus is to account for the variability in HRF that can be observed in
454 different regions of the brain. First, variability in the temporal characteristics of the HRF can arise
455 from differences in stimulus intensity and patterns, as well as with short inter-event intervals like
456 in fast cognitive processes or experimental designs (Yesilyurt et al., 2008; Sadaghiani et al., 2009;
457 Chen et al., 2021; Polimeni and Lewis, 2021). Similarly, the HRF shape at rest might differ from the
458 canonical HRF commonly used for task-based fMRI data analysis. A wide variety of HRF patterns
459 could be elicited across the whole brain and possible detected with sufficiently large signal-to-noise
460 ratio, e.g., (Gonzalez-Castillo et al., 2012) showed two gamma-shaped responses at the onset and

461 the end of the evoked trial, respectively. This unique HRF shape would be deconvolved as two
462 separate events with the conventional deconvolution techniques. The impact of HRF variability
463 could be reduced using structured regularization terms along with multiple basis functions (Gaudes
464 et al., 2012) or procedures that estimate the HRF shape in an adaptive fashion in both analysis
465 (Farouj et al., 2019) and synthesis formulations (Cherkaoui et al., 2020a).

466 Another avenue of research consists in leveraging spatial information by adopting multivariate
467 deconvolution approaches that operate at the whole-brain level, instead of working voxelwise and
468 beyond regional regularization terms (e.g. as proposed in Karahanoglu et al. 2013). Operating
469 at the whole-brain level would open the way for methods that consider shared neuronal activity
470 using mixed norm regularization terms (Uruñuela-Tremiño et al., 2019) or can capture long-range
471 neuronal cofluctuations using low rank decompositions (Cherkaoui et al., 2020a). For example,
472 multivariate deconvolution approaches could yield better localized activity patterns while reducing
473 the effect of global fluctuations such as respiratory artifacts, which cannot be modelled at the voxel
474 level (Uruñuela et al., 2021).

475 Similar to solving other inverse problems by means of regularized estimators, the selection of
476 the regularization parameter is critical to correctly estimate the neuronal-related signal. Hence,
477 methods that take advantage of a more robust selection of the regularization parameter could
478 considerably yield more reliable estimates of the neuronal-related signal. For instance, the stability
479 selection (Meinshausen and Bühlmann, 2010; Uruñuela et al., 2020) procedure could be included
480 to the deconvolution problem to ensure that the estimated coefficients are obtained with high
481 probability. Furthermore, an important issue of regularized estimation is that the estimates are
482 biased with respect to the true value. In that sense, the use of non-convex $\ell_{p,q}$ -norm regularization
483 terms (e.g., $p < 1$) can reduce this bias while maintaining the sparsity constraint, at the cost of
484 potentially converging to a local minima of the regularized estimation problem. In practice, these
485 approaches could avoid the optional debiasing step that overcomes the shrinkage of the estimates and
486 obtain a more accurate and less biased fit of the fMRI signal (Gaudes et al., 2013; Caballero-Gaudes
487 et al., 2019). Finally, cutting-edge developments on physics-informed deep learning techniques
488 for inverse problems (Akçakaya et al., 2021; Monga et al., 2021; Ongie et al., 2020; Cherkaoui
489 et al., 2020b) could be transferred for deconvolution by considering the biophysical model of the
490 hemodynamic system and could potentially offer algorithms with reduced computational time and
491 more flexibility.

492 6. Code and data availability

493 The code and materials used in this work can be found in the following GitHub repository:
494 https://github.com/eurunuela/pfm_vs_ta. We encourage the reader to explore the parameters
495 (e.g., SNR, varying HRF options and mismatch between algorithms, TR, number of events, onsets,
496 and durations) in the provided Jupyter notebooks. Likewise, the data used to produce the figures
497 can be found in <https://osf.io/f3ryg/>.

498 7. Acknowledgements

499 We thank Stefano Moia and Vicente Ferrer for data availability, and Younes Farouj for valuable
500 comments on the manuscript. This research was funded by the Spanish Ministry of Economy and
501 Competitiveness (RYC-2017-21845), the Basque Government (BERC 2018-2021, PIB_2019_104,
502 PRE_2020_2_0227), and the Spanish Ministry of Science, Innovation and Universities (PID2019-
503 105520GB-100), and the Swiss National Science Foundation (grant 205321_163376).

504 **8. CRediT**

505 Eneko Uruñuela: Conceptualisation, Methodology, Software, Formal Analysis, Investigation,
506 Data Curation, Writing (OD), Writing (RE), Visualisation, Funding acquisition. Thomas A.W.
507 Bolton: Conceptualisation, Methodology, Writing (RE). Dimitri Van de Ville: Conceptualisation,
508 Methodology, Writing (RE). César Caballero-Gaudes: Conceptualisation, Methodology, Software,
509 Formal Analysis, Investigation, Data Curation, Writing (OD), Writing (RE), Visualisation, Funding
510 acquisition.

511 **References**

- 512 Akçakaya, M., Yaman, B., Chung, H., Ye, J.C., 2021. Unsupervised deep learning methods for
513 biological image reconstruction [arXiv:2105.08040](https://arxiv.org/abs/2105.08040).
- 514 Allan, T.W., Francis, S.T., Caballero-Gaudes, C., Morris, P.G., Liddle, E.B., Liddle, P.F., Brookes,
515 M.J., Gowland, P.A., 2015. Functional connectivity in MRI is driven by spontaneous BOLD
516 events. *PLOS ONE* 10, e0124577. doi:10.1371/journal.pone.0124577.
- 517 Andersson, J.L., Skare, S., Ashburner, J., 2003. How to correct susceptibility distortions in spin-
518 echo echo-planar images: application to diffusion tensor imaging. *NeuroImage* 20, 870–888.
519 doi:10.1016/s1053-8119(03)00336-7.
- 520 Aslan, S., Cemgil, A.T., Akin, A., 2016. Joint state and parameter estimation of the hemodynamic
521 model by particle smoother expectation maximization method. *Journal of Neural Engineering*
522 13, 046010. doi:10.1088/1741-2560/13/4/046010.
- 523 Beck, A., Teboulle, M., 2009. A fast iterative shrinkage-thresholding algorithm for linear inverse
524 problems. *SIAM Journal on Imaging Sciences* 2, 183–202. doi:10.1137/080716542.
- 525 Behzadi, Y., Restom, K., Liau, J., Liu, T.T., 2007. A component based noise correction method
526 (CompCor) for BOLD and perfusion based fMRI. *NeuroImage* 37, 90–101. doi:10.1016/j.
527 neuroimage.2007.04.042.
- 528 Birn, R.M., Diamond, J.B., Smith, M.A., Bandettini, P.A., 2006. Separating respiratory-variation-
529 related fluctuations from neuronal-activity-related fluctuations in fMRI. *NeuroImage* 31, 1536–
530 1548. doi:10.1016/j.neuroimage.2006.02.048.
- 531 Bolton, T.A., Morgenroth, E., Preti, M.G., Ville, D.V.D., 2020. Tapping into multi-faceted human
532 behavior and psychopathology using fMRI brain dynamics. *Trends in Neurosciences* 43, 667–680.
533 doi:10.1016/j.tins.2020.06.005.
- 534 Bommarito, G., Tarun, A., Farouj, Y., Preti, M.G., Petracca, M., Droby, A., Mendili, M.M.E.,
535 Inglese, M., Ville, D.V.D., 2020. Altered anterior default mode network dynamics in progressive
536 multiple sclerosis. *medRxiv* doi:10.1101/2020.11.26.20238923.
- 537 Bommarito, G., Tarun, A., Farouj, Y., Preti, M.G., Petracca, M., Droby, A., Mounir El Mendili,
538 M., Inglese, M., Van De Ville, D., in press. Altered anterior default mode network dynamics in
539 progressive multiple sclerosis. *Multiple Sclerosis Journal* doi:10.1177/13524585211018116.

- 540 Boynton, G.M., Engel, S.A., Glover, G.H., Heeger, D.J., 1996. Linear systems analysis of functional
541 magnetic resonance imaging in human v1. *The Journal of Neuroscience* 16, 4207–4221. doi:10.
542 1523/jneurosci.16-13-04207.1996.
- 543 Bruckstein, A.M., Donoho, D.L., Elad, M., 2009. From sparse solutions of systems of equations to
544 sparse modeling of signals and images. *SIAM Review* 51, 34–81. doi:10.1137/060657704.
- 545 Bush, K., Cisler, J., 2013. Decoding neural events from fMRI BOLD signal: A comparison of
546 existing approaches and development of a new algorithm. *Magnetic Resonance Imaging* 31, 976–
547 989. doi:10.1016/j.mri.2013.03.015.
- 548 Bush, K., Zhou, S., Cisler, J., Bian, J., Hazaroglu, O., Gillispie, K., Yoshigoe, K., Kilts, C.,
549 2015. A deconvolution-based approach to identifying large-scale effective connectivity. *Magnetic*
550 *Resonance Imaging* 33, 1290–1298. doi:10.1016/j.mri.2015.07.015.
- 551 Buxton, R.B., Wong, E.C., Frank, L.R., 1998. Dynamics of blood flow and oxygenation changes
552 during brain activation: the balloon model. *Magnetic resonance in medicine* 39, 855–864.
- 553 Caballero-Gaudes, C., Moia, S., Panwar, P., Bandettini, P.A., Gonzalez-Castillo, J., 2019. A
554 deconvolution algorithm for multi-echo functional MRI: Multi-echo sparse paradigm free mapping.
555 *NeuroImage* 202, 116081. doi:10.1016/j.neuroimage.2019.116081.
- 556 Casanova, R., Ryali, S., Serences, J., Yang, L., Kraft, R., Laurienti, P.J., Maldjian, J.A., 2008. The
557 impact of temporal regularization on estimates of the BOLD hemodynamic response function: A
558 comparative analysis. *NeuroImage* 40, 1606–1618. doi:10.1016/j.neuroimage.2008.01.011.
- 559 Chambolle, A., 2004. An algorithm for total variation minimization and applications. *Journal of*
560 *Mathematical imaging and vision* 20, 89–97.
- 561 Chen, J.E., Glover, G.H., Fultz, N.E., Rosen, B.R., Polimeni, J.R., Lewis, L.D., 2021. Investigating
562 mechanisms of fast BOLD responses: The effects of stimulus intensity and of spatial heterogeneity
563 of hemodynamics. *NeuroImage* 245, 118658. doi:10.1016/j.neuroimage.2021.118658.
- 564 Chen, S.S., Donoho, D.L., Saunders, M.A., 2001. Atomic decomposition by basis pursuit. *SIAM*
565 *review* 43, 129–159.
- 566 Cherkaoui, H., Moreau, T., Halimi, A., Ciuciu, P., 2019. Sparsity-based blind deconvolution of
567 neural activation signal in FMRI, in: ICASSP 2019 - 2019 IEEE International Conference on
568 Acoustics, Speech and Signal Processing (ICASSP), IEEE. pp. 1323–1327. doi:10.1109/icassp.
569 2019.8683358.
- 570 Cherkaoui, H., Moreau, T., Halimi, A., Leroy, C., Ciuciu, P., 2020a. Multivariate semi-blind
571 deconvolution of fMRI time series. URL: <https://hal.archives-ouvertes.fr/hal-03005584>.
572 working paper or preprint.
- 573 Cherkaoui, H., Sulam, J., Moreau, T., 2020b. Learning to solve TV regularised problems with
574 unrolled algorithms 33, 11513–11524. URL: <https://proceedings.neurips.cc/paper/2020/file/84fec9a8e45846340fdf5c7c9f7ed66c-Paper.pdf>.
- 576 Cifre, I., Flores, M.T.M., Ochab, J.K., Chialvo, D.R., 2020a. Revisiting non-linear functional brain
577 co-activations: directed, dynamic and delayed. *arXiv:2007.15728*.

- 578 Cifre, I., Zarepour, M., Horovitz, S.G., Cannas, S.A., Chialvo, D.R., 2020b. Further results on why
579 a point process is effective for estimating correlation between brain regions. *Papers in Physics*
580 12, 120003. doi:10.4279/pip.120003.
- 581 Ciuciu, P., Poline, J.B., Marrelec, G., Idier, J., Pallier, C., Benali, H., 2003. Unsupervised robust
582 nonparametric estimation of the hemodynamic response function for any fmri experiment. *IEEE*
583 *transactions on medical imaging* 22, 1235–1251. doi:10.1109/TMI.2003.817759.
- 584 Cohen, M.S., 1997. Parametric analysis of fMRI data using linear systems methods. *NeuroImage*
585 6, 93–103. doi:10.1006/nimg.1997.0278.
- 586 Costantini, I., Deriche, R., Deslauriers-Gauthier, S., 2021. A paradigm free regularization approach
587 to recover brain activation from functional MRI data. *bioRxiv* doi:10.1101/2021.04.14.438942.
- 588 Cox, R.W., 1996. AFNI: Software for analysis and visualization of functional magnetic resonance
589 neuroimages. *Computers and Biomedical Research* 29, 162–173. doi:10.1006/cbmr.1996.0014.
- 590 Deco, G., Kringelbach, M.L., 2017. Hierarchy of information processing in the brain: A novel
591 ‘intrinsic ignition’ framework. *Neuron* 94, 961–968. doi:10.1016/j.neuron.2017.03.028.
- 592 Deco, G., Tagliazucchi, E., Laufs, H., Sanjuán, A., Kringelbach, M.L., 2017. Novel intrinsic ignition
593 method measuring local-global integration characterizes wakefulness and deep sleep. *eNeuro* 4.
594 doi:10.1523/ENEURO.0106-17.2017.
- 595 Di, X., Biswal, B.B., 2013. Modulatory interactions of resting-state brain functional connectivity.
596 *PLoS ONE* 8, e71163. doi:10.1371/journal.pone.0071163.
- 597 Di, X., Biswal, B.B., 2015. Characterizations of resting-state modulatory interactions in the human
598 brain. *Journal of Neurophysiology* 114, 2785–2796. doi:10.1152/jn.00893.2014.
- 599 Di, X., Biswal, B.B., 2018. Toward task connectomics: Examining whole-brain task modulated
600 connectivity in different task domains. *Cerebral Cortex* 29, 1572–1583. doi:10.1093/cercor/
601 bhy055.
- 602 Efron, B., Hastie, T., Johnstone, I., Tibshirani, R., 2004. Least angle regression. *The Annals of*
603 *Statistics* 32, 407–499. doi:10.1214/009053604000000067.
- 604 Elad, M., Milanfar, P., Rubinstein, R., 2007. Analysis versus synthesis in signal priors. *Inverse*
605 *Problems* 23, 947–968. doi:10.1088/0266-5611/23/3/007.
- 606 Esfahlani, F.Z., Jo, Y., Faskowitz, J., Byrge, L., Kennedy, D.P., Sporns, O., Betzel, R.F., 2020.
607 High-amplitude cofluctuations in cortical activity drive functional connectivity. *Proceedings of*
608 *the National Academy of Sciences* 117, 28393–28401. doi:10.1073/pnas.2005531117.
- 609 Farouj, Y., Karahanoglu, F.I., Ville, D.V.D., 2019. Bold signal deconvolution under uncertain
610 hÆmodynamics: A semi-blind approach, in: 2019 IEEE 16th International Symposium on
611 Biomedical Imaging (ISBI 2019), IEEE. IEEE. pp. 1792–1796. doi:10.1109/isbi.2019.8759248.
- 612 Farouj, Y., Karahanoglu, F.I., Ville, D.V.D., 2020. Deconvolution of sustained neural activity from
613 large-scale calcium imaging data 39, 1094–1103. doi:10.1109/tmi.2019.2942765.

- 614 Faskowitz, J., Esfahlani, F.Z., Jo, Y., Sporns, O., Betzel, R.F., 2020. Edge-centric functional
615 network representations of human cerebral cortex reveal overlapping system-level architecture.
616 *Nature neuroscience* 23, 1644–1654. doi:10.1038/s41593-020-00719-y.
- 617 Feinberg, D.A., Moeller, S., Smith, S.M., Auerbach, E., Ramanna, S., Glasser, M.F., Miller, K.L.,
618 Ugurbil, K., Yacoub, E., 2010. Multiplexed echo planar imaging for sub-second whole brain
619 fMRI and fast diffusion imaging. *PLoS ONE* 5, e15710. doi:10.1371/journal.pone.0015710.
- 620 Freitas, L.G., Bolton, T.A., Krikler, B.E., Jochaut, D., Giraud, A.L., Hüppi, P.S., Ville, D.V.D.,
621 2020. Time-resolved effective connectivity in task fMRI: Psychophysiological interactions of co-
622 activation patterns. *NeuroImage* 212, 116635. doi:10.1016/j.neuroimage.2020.116635.
- 623 Friedrich, J., Zhou, P., Paninski, L., 2017. Fast online deconvolution of calcium imaging data.
624 *PLOS Computational Biology* 13, e1005423. doi:10.1371/journal.pcbi.1005423.
- 625 Friston, K., Fletcher, P., Josephs, O., Holmes, A., Rugg, M., Turner, R., 1998. Event-related fMRI:
626 Characterizing differential responses. *NeuroImage* 7, 30–40. doi:10.1006/nimg.1997.0306.
- 627 Friston, K., Trujillo-Barreto, N., Daunizeau, J., 2008. DEM: A variational treatment of dynamic
628 systems. *NeuroImage* 41, 849–885. doi:10.1016/j.neuroimage.2008.02.054.
- 629 Friston, K.J., Jezzard, P., Turner, R., 1994. Analysis of functional MRI time-series. *Human Brain
630 Mapping* 1, 153–171. doi:10.1002/hbm.460010207.
- 631 Friston, K.J., Mechelli, A., Turner, R., Price, C.J., 2000. Nonlinear responses in fmri: the balloon
632 model, volterra kernels, and other hemodynamics. *NeuroImage* 12, 466–477.
- 633 Gaudes, C.C., Karahanoglu, F.I., Lazeyras, F., Ville, D.V.D., 2012. Structured sparse deconvolution
634 for paradigm free mapping of functional MRI data, in: 2012 9th IEEE International Symposium
635 on Biomedical Imaging (ISBI), IEEE. IEEE. pp. 322–325. doi:10.1109/isbi.2012.6235549.
- 636 Gaudes, C.C., Petridou, N., Dryden, I.L., Bai, L., Francis, S.T., Gowland, P.A., 2010. Detection
637 and characterization of single-trial fMRI bold responses: Paradigm free mapping. *Human Brain
638 Mapping* 32, 1400–1418. doi:10.1002/hbm.21116.
- 639 Gaudes, C.C., Petridou, N., Francis, S.T., Dryden, I.L., Gowland, P.A., 2013. Paradigm free
640 mapping with sparse regression automatically detects single-trial functional magnetic resonance
641 imaging blood oxygenation level dependent responses. *Human Brain Mapping* , n/a–n/adoi:10.
642 1002/hbm.21452.
- 643 Gaudes, C.C., Van De Ville, D., Petridou, N., Lazeyras, F., Gowland, P., 2011. Paradigm-free
644 mapping with morphological component analysis: Getting most out of fmri data, in: Wavelets
645 and Sparsity XIV, International Society for Optics and Photonics. p. 81381K.
- 646 Gerchen, M.F., Bernal-Casas, D., Kirsch, P., 2014. Analyzing task-dependent brain network changes
647 by whole-brain psychophysiological interactions: A comparison to conventional analysis. *Human
648 Brain Mapping* 35, 5071–5082. doi:10.1002/hbm.22532.
- 649 Gitelman, D.R., Penny, W.D., Ashburner, J., Friston, K.J., 2003. Modeling regional and psy-
650 chophysiologic interactions in fMRI: the importance of hemodynamic deconvolution. *NeuroImage*
651 19, 200–207. doi:10.1016/s1053-8119(03)00058-2.

- 652 Glasser, M.F., Smith, S.M., Marcus, D.S., Andersson, J.L.R., Auerbach, E.J., Behrens, T.E.J.,
653 Coalson, T.S., Harms, M.P., Jenkinson, M., Moeller, S., Robinson, E.C., Sotiroopoulos, S.N., Xu,
654 J., Yacoub, E., Ugurbil, K., Essen, D.C.V., 2016. The human connectome project's neuroimaging
655 approach. *Nature Neuroscience* 19, 1175–1187. doi:10.1038/nn.4361.
- 656 Glover, G.H., 1999. Deconvolution of impulse response in event-related BOLD fMRI1. *NeuroImage*
657 9, 416–429. doi:10.1006/nimg.1998.0419.
- 658 Gonzalez-Castillo, J., Caballero-Gaudes, C., Topolski, N., Handwerker, D.A., Pereira, F., Ban-
659 dettini, P.A., 2019. Imaging the spontaneous flow of thought: Distinct periods of cogni-
660 tion contribute to dynamic functional connectivity during rest. *NeuroImage* 202, 116129.
661 doi:10.1016/j.neuroimage.2019.116129.
- 662 Gonzalez-Castillo, J., Saad, Z.S., Handwerker, D.A., Inati, S.J., Brenowitz, N., Bandettini, P.A.,
663 2012. Whole-brain, time-locked activation with simple tasks revealed using massive averaging
664 and model-free analysis. *Proceedings of the National Academy of Sciences of the United States
665 of America* 109, 5487–5492. doi:10.1073/pnas.1121049109.
- 666 Goutte, C., Nielsen, F.A., Hansen, L.K., 2000. Modeling the haemodynamic response in fmri using
667 smooth fir filters. *IEEE transactions on medical imaging* 19, 1188–1201. doi:10.1109/42.897811.
- 668 Havlicek, M., Friston, K.J., Jan, J., Brazdil, M., Calhoun, V.D., 2011. Dynamic modeling of
669 neuronal responses in fMRI using cubature kalman filtering. *NeuroImage* 56, 2109–2128. doi:10.
670 1016/j.neuroimage.2011.03.005.
- 671 Henson, R., Friston, K., 2007. Chapter 14 - convolution models for fmri, in: Friston, K., Ash-
672 burner, J., Kiebel, S., Nichols, T., Penny, W. (Eds.), *Statistical Parametric Mapping*. Academic
673 Press, London, pp. 178–192. URL: <https://www.sciencedirect.com/science/article/pii/B9780123725608500140>, doi:<https://doi.org/10.1016/B978-012372560-8/50014-0>.
- 675 Hernandez-Garcia, L., Ulfarsson, M.O., 2011. Neuronal event detection in fMRI time series using
676 iterative deconvolution techniques. *Magnetic Resonance Imaging* 29, 353–364. doi:10.1016/j.
677 mri.2010.10.012.
- 678 Hütel, M., Antonelli, M., Melbourne, A., Ourselin, S., 2021. Hemodynamic matrix factorization for
679 functional magnetic resonance imaging. *NeuroImage* 231, 117814. doi:10.1016/j.neuroimage.
680 2021.117814.
- 681 Hütel, M., Melbourne, A., Ourselin, S., 2018. Neural activation estimation in brain networks
682 during task and rest using BOLD-fMRI, in: *Medical Image Computing and Computer Assisted
683 Intervention – MICCAI 2018*, Springer. Springer International Publishing. pp. 215–222. doi:10.
684 1007/978-3-030-00931-1_25.
- 685 Jenkinson, M., Beckmann, C.F., Behrens, T.E., Woolrich, M.W., Smith, S.M., 2012. FSL. *Neu-
686 roImage* 62, 782–790. doi:10.1016/j.neuroimage.2011.09.015.
- 687 Jenkinson, M., Smith, S., 2001. A global optimisation method for robust affine registration of brain
688 images. *Medical Image Analysis* 5, 143–156. doi:10.1016/s1361-8415(01)00036-6.
- 689 Jewell, S.W., Hocking, T.D., Fearnhead, P., Witten, D.M., 2019. Fast nonconvex deconvolution of
690 calcium imaging data. *Biostatistics* 21, 709–726. doi:10.1093/biostatistics/kxy083.

- 691 Jo, Y., Faskowitz, J., Esfahlani, F.Z., Sporns, O., Betzel, R.F., 2021. Subject identification us-
692 ing edge-centric functional connectivity. *NeuroImage* 238, 118204. doi:10.1016/j.neuroimage.
693 2021.118204.
- 694 Karahanoglu, F.I., Bayram, İ., Ville, D.V.D., 2011. A signal processing approach to generalized
695 1-d total variation. *IEEE Transactions on Signal Processing* 59, 5265–5274. doi:10.1109/tsp.
696 2011.2164399.
- 697 Karahanoglu, F.I., Caballero-Gaudes, C., Lazeyras, F., Ville, D.V.D., 2013. Total activation: fMRI
698 deconvolution through spatio-temporal regularization. *NeuroImage* 73, 121–134. doi:10.1016/
699 j.neuroimage.2013.01.067.
- 700 Karahanoglu, F.I., Grouiller, F., Gaudes, C.C., Seeck, M., Vulliemoz, S., Ville, D.V.D., 2013.
701 Spatial mapping of interictal epileptic discharges in fMRI with total activation, in: 2013 IEEE
702 10th International Symposium on Biomedical Imaging, Ieee. IEEE. pp. 1500–1503. doi:10.1109/
703 isbi.2013.6556819.
- 704 Karahanoglu, F.I., Ville, D.V.D., 2015. Transient brain activity disentangles fMRI resting-state
705 dynamics in terms of spatially and temporally overlapping networks. *Nature Communications* 6,
706 7751. doi:10.1038/ncomms8751.
- 707 Karahanoglu, F.I., Ville, D.V.D., 2017. Dynamics of large-scale fMRI networks: Deconstruct brain
708 activity to build better models of brain function. *Current Opinion in Biomedical Engineering* 3,
709 28–36. doi:10.1016/j.cobme.2017.09.008.
- 710 Keilholz, S., Caballero-Gaudes, C., Bandettini, P., Deco, G., Calhoun, V., 2017. Time-resolved
711 resting-state functional magnetic resonance imaging analysis: Current status, challenges, and
712 new directions. *Brain Connectivity* 7, 465–481. doi:10.1089/brain.2017.0543.
- 713 Khalidov, I., Fadili, J., Lazeyras, F., Ville, D.V.D., Unser, M., 2011. Activelets: Wavelets for
714 sparse representation of hemodynamic responses. *Signal Processing* 91, 2810–2821. doi:10.1016/
715 j.sigpro.2011.03.008.
- 716 Kinany, N., Pirondini, E., Micera, S., Ville, D.V.D., 2020. Dynamic functional connectivity of
717 resting-state spinal cord fMRI reveals fine-grained intrinsic architecture. *Neuron* 108, 424–435.e4.
718 doi:10.1016/j.neuron.2020.07.024.
- 719 Lindquist, M.A., Waugh, C., Wager, T.D., 2007. Modeling state-related fMRI activity using change-
720 point theory. *NeuroImage* 35, 1125–1141. doi:10.1016/j.neuroimage.2007.01.004.
- 721 Liu, X., Chang, C., Duyn, J.H., 2013. Decomposition of spontaneous brain activity into distinct
722 fMRI co-activation patterns. *Frontiers in Systems Neuroscience* 7, 101. doi:10.3389/fnsys.
723 2013.00101.
- 724 Liu, X., Duyn, J.H., 2013. Time-varying functional network information extracted from brief
725 instances of spontaneous brain activity. *Proceedings of the National Academy of Sciences* 110,
726 4392–4397. doi:10.1073/pnas.1216856110.
- 727 Liu, X., Zhang, N., Chang, C., Duyn, J.H., 2018. Co-activation patterns in resting-state fMRI
728 signals. *NeuroImage* 180, 485–494. doi:10.1016/j.neuroimage.2018.01.041.

- 729 Lopes, R., Lina, J., Fahoum, F., Gotman, J., 2012. Detection of epileptic activity in fMRI without
730 recording the EEG. *NeuroImage* 60, 1867–1879. doi:10.1016/j.neuroimage.2011.12.083.
- 731 Loula, J., Varoquaux, G., Thirion, B., 2018. Decoding fMRI activity in the time domain improves
732 classification performance. *NeuroImage* 180, 203–210. doi:10.1016/j.neuroimage.2017.08.018.
- 733 Lurie, D.J., Kessler, D., Bassett, D.S., Betzel, R.F., Breakspear, M., Kheilholz, S., Kucyi, A.,
734 Liégeois, R., Lindquist, M.A., McIntosh, A.R., Poldrack, R.A., Shine, J.M., Thompson, W.H.,
735 Bielczyk, N.Z., Douw, L., Kraft, D., Miller, R.L., Muthuraman, M., Pasquini, L., Razi, A.,
736 Vidaurre, D., Xie, H., Calhoun, V.D., 2020. Questions and controversies in the study of time-
737 varying functional connectivity in resting fMRI. *Network Neuroscience* 4, 30–69. doi:10.1162/
738 *netn_a_00116*.
- 739 Madi, M.K., Karameh, F.N., 2017. Hybrid cubature kalman filtering for identifying nonlinear
740 models from sampled recording: Estimation of neuronal dynamics. *PLOS ONE* 12, e0181513.
741 doi:10.1371/journal.pone.0181513.
- 742 Marrelec, G., Benali, H., Ciuci, P., Poline, J.B., 2002. Bayesian estimation of the hemo-
743 dynamic response function in functional mri. *AIP Conference Proceedings* 617, 229–247.
744 URL: <https://aip.scitation.org/doi/abs/10.1063/1.1477050>, doi:10.1063/1.1477050,
745 arXiv:<https://aip.scitation.org/doi/pdf/10.1063/1.1477050>.
- 746 Meinshausen, N., Bühlmann, P., 2010. Stability selection. *Journal of the Royal Statistical Society:*
747 *Series B (Statistical Methodology)* 72, 417–473. doi:10.1111/j.1467-9868.2010.00740.x.
- 748 Moeller, S., Yacoub, E., Olman, C.A., Auerbach, E., Strupp, J., Harel, N., Uğurbil, K., 2010.
749 Multiband multislice GE-EPI at 7 tesla, with 16-fold acceleration using partial parallel imaging
750 with application to high spatial and temporal whole-brain fMRI. *Magnetic Resonance in Medicine*
751 63, 1144–1153. doi:10.1002/mrm.22361.
- 752 Monga, V., Li, Y., Eldar, Y.C., 2021. Algorithm unrolling: Interpretable, efficient deep learning
753 for signal and image processing. *IEEE Signal Processing Magazine* 38, 18–44. doi:10.1109/MSP.
754 2020.3016905.
- 755 Ongie, G., Jalal, A., Metzler, C.A., Baraniuk, R.G., Dimakis, A.G., Willett, R., 2020. Deep learning
756 techniques for inverse problems in imaging. *IEEE Journal on Selected Areas in Information
757 Theory* 1, 39–56. doi:10.1109/JSAIT.2020.2991563.
- 758 van Oort, E.S.B., Mennes, M., Navarro Schröder, T., Kumar, V.J., Zaragoza Jimenez, N.I., Grodd,
759 W., Doeller, C.F., Beckmann, C.F., 2018. Functional parcellation using time courses of instan-
760 taneous connectivity. *NeuroImage* 170, 31–40. doi:10.1016/j.neuroimage.2017.07.027.
- 761 Ortelli, F., van de Geer, S., 2019. Synthesis and analysis in total variation regularization.
762 arXiv:1901.06418.
- 763 Patriat, R., Molloy, E.K., Birn, R.M., 2015. Using edge voxel information to improve motion
764 regression for rs-fMRI connectivity studies. *Brain Connectivity* 5, 582–595. doi:10.1089/brain.
765 2014.0321.
- 766 Penny, W., Ghahramani, Z., Friston, K., 2005. Bilinear dynamical systems. *Philosophical Trans-
767 actions of the Royal Society B: Biological Sciences* 360, 983–993. doi:10.1098/rstb.2005.1642.

- 768 Petridou, N., Gaudes, C.C., Dryden, I.L., Francis, S.T., Gowland, P.A., 2012. Periods of rest in
769 fMRI contain individual spontaneous events which are related to slowly fluctuating spontaneous
770 activity. *Human Brain Mapping* 34, 1319–1329. doi:10.1002/hbm.21513.
- 771 Pidnebesna, A., Fajnerová, I., Horáček, J., Hlinka, J., 2019. Estimating sparse neuronal signal from
772 hemodynamic response: the mixture components inference approach. *bioRxiv* doi:10.1101/2019.
773 12.19.876508.
- 774 Pirondini, E., Kinany, N., Sueur, C.L., Griffis, J.C., Shulman, G.L., Corbetta, M., Ville, D.V.D.,
775 2022. Post-stroke reorganization of transient brain activity characterizes deficits and recovery of
776 cognitive functions. *NeuroImage* 255, 119201. doi:10.1016/j.neuroimage.2022.119201.
- 777 Polimeni, J.R., Lewis, L.D., 2021. Imaging faster neural dynamics with fast fmri: A need for
778 updated models of the hemodynamic response. *Progress in neurobiology* 207, 102174. doi:10.
779 1016/j.pneurobio.2021.102174.
- 780 Posse, S., Wiese, S., Gembris, D., Mathiak, K., Kessler, C., Grosse-Ruyken, M.L., Elghahwagi,
781 B., Richards, T., Dager, S.R., Kiselev, V.G., 1999. Enhancement of BOLD-contrast sensitivity
782 by single-shot multi-echo functional MR imaging. *Magnetic Resonance in Medicine* 42, 87–97.
783 doi:10.1002/(sici)1522-2594(199907)42:1<87::aid-mrm13>3.0.co;2-o.
- 784 Preti, M.G., Bolton, T.A., Ville, D.V.D., 2017. The dynamic functional connectome: State-of-the-
785 art and perspectives. *NeuroImage* 160, 41–54. doi:10.1016/j.neuroimage.2016.12.061.
- 786 Raguet, H., Fadili, J., Peyré, G., 2013. A generalized forward-backward splitting. *SIAM Journal*
787 on Imaging Sciences 6, 1199–1226. doi:10.1137/120872802.
- 788 Riera, J.J., Watanabe, J., Kazuki, I., Naoki, M., Aubert, E., Ozaki, T., Kawashima, R., 2004. A
789 state-space model of the hemodynamic approach: nonlinear filtering of BOLD signals. *NeuroIm-*
790 *age* 21, 547–567. doi:10.1016/j.neuroimage.2003.09.052.
- 791 Rolls, E.T., Cheng, W., Feng, J., 2021. Brain dynamics: Synchronous peaks, functional connectivity,
792 and its temporal variability. *Human brain mapping* 42, 2790–2801. doi:10.1002/hbm.25404.
- 793 Ruiz-Euler, H.C., Marques, J.R.F., Kappen, H.J., 2018. Nonlinear deconvolution by sampling
794 biophysically plausible hemodynamic models. *arXiv:1803.08797*.
- 795 Sadaghiani, S., Uğurbil, K., Uludağ, K., 2009. Neural activity-induced modulation of bold poststim-
796 ulus undershoot independent of the positive signal. *Magnetic resonance imaging* 27, 1030–1038.
797 doi:10.1016/j.mri.2009.04.003.
- 798 Schwarz, G., 1978. Estimating the dimension of a model. *The Annals of Statistics* 6, 461–464.
799 doi:10.1214/aos/1176344136.
- 800 Setsompop, K., Gagoski, B.A., Polimeni, J.R., Witzel, T., Wedeen, V.J., Wald, L.L., 2011. Blipped-
801 controlled aliasing in parallel imaging for simultaneous multislice echo planar imaging with re-
802 duced g -factor penalty. *Magnetic Resonance in Medicine* 67, 1210–1224. doi:10.1002/mrm.23097.
- 803 Shmueli, K., van Gelderen, P., de Zwart, J.A., Horovitz, S.G., Fukunaga, M., Jansma, J.M., Duyn,
804 J.H., 2007. Low-frequency fluctuations in the cardiac rate as a source of variance in the resting-
805 state fMRI BOLD signal. *NeuroImage* 38, 306–320. doi:10.1016/j.neuroimage.2007.07.037.

- 806 Sporns, O., Faskowitz, J., Teixeira, A.S., Cutts, S.A., Betzel, R.F., 2021. Dynamic expression of
807 brain functional systems disclosed by fine-scale analysis of edge time series. *Network neuroscience*
808 (Cambridge, Mass.) 5, 405–433. doi:10.1162/netn_a_00182.
- 809 Sreenivasan, K.R., Havlicek, M., Deshpande, G., 2015. Nonparametric hemodynamic deconvolution
810 of fMRI using homomorphic filtering. *IEEE Transactions on Medical Imaging* 34, 1155–1163.
811 doi:10.1109/tmi.2014.2379914.
- 812 Tagliazucchi, E., Balenzuela, P., Fraiman, D., Chialvo, D.R., 2012. Criticality in large-scale brain
813 fmri dynamics unveiled by a novel point process analysis. *Frontiers in physiology* 3, 15. doi:10.
814 3389/fphys.2012.00015.
- 815 Tagliazucchi, E., Balenzuela, P., Fraiman, D., Montoya, P., Chialvo, D.R., 2011. Spontaneous bold
816 event triggered averages for estimating functional connectivity at resting state. *Neuroscience
817 letters* 488, 158–163. doi:10.1016/j.neulet.2010.11.020.
- 818 Tagliazucchi, E., Siniatchkin, M., Laufs, H., Chialvo, D.R., 2016. The voxel-wise functional
819 connectome can be efficiently derived from co-activations in a sparse spatio-temporal point-process.
820 *Frontiers in neuroscience* 10, 381. doi:10.3389/fnins.2016.00381.
- 821 Tan, F.M., Caballero-Gaudes, C., Mullinger, K.J., Cho, S.Y., Zhang, Y., Dryden, I.L., Francis,
822 S.T., Gowland, P.A., 2017. Decoding fMRI events in sensorimotor motor network using sparse
823 paradigm free mapping and activation likelihood estimates. *Human Brain Mapping* 38, 5778–
824 5794. doi:10.1002/hbm.23767.
- 825 Tarun, A., Wainstein-Andriano, D., Sterpenich, V., Bayer, L., Perogamvros, L., Solms, M., Ax-
826 macher, N., Schwartz, S., Ville, D.V.D., 2020. NREM sleep stages specifically alter dynamical
827 integration of large-scale brain networks. *iScience* 24, 101923. doi:10.1101/2020.07.08.193508.
- 828 Tarun, A., Wainstein-Andriano, D., Sterpenich, V., Bayer, L., Perogramvos, L., Solms, M., Ax-
829 macher, N., Schwartz, S., Van De Ville, D., 2021. NREM sleep stages specifically alter dynamical
830 integration of large-scale brain networks. *iScience* 24, 101923. doi:10.1016/j.isci.2020.101923.
- 831 Tibshirani, R., 1996. Regression shrinkage and selection via the lasso. *Journal of the Royal Statistical
832 Society: Series B (Methodological)* 58, 267–288. doi:10.1111/j.2517-6161.1996.tb02080.x.
- 833 Triantafyllou, C., Hoge, R., Krueger, G., Wiggins, C., Potthast, A., Wiggins, G., Wald, L., 2005.
834 Comparison of physiological noise at 1.5 t, 3 t and 7 t and optimization of fMRI acquisition
835 parameters. *NeuroImage* 26, 243–250. doi:10.1016/j.neuroimage.2005.01.007.
- 836 Uruñuela, E., Jones, S., Crawford, A., Shin, W., Oh, S., Lowe, M., Caballero-Gaudes, C., 2020.
837 Stability-based sparse paradigm free mapping algorithm for deconvolution of functional MRI
838 data. *Proceedings of the Annual International Conference of the IEEE Engineering in Medicine
839 and Biology Society, EMBS 2020-July*, 1092–1095. doi:10.1109/embc44109.2020.9176137.
- 840 Uruñuela, E., Moia, S., Caballero-Gaudes, C., 2021. A low rank and sparse paradigm free mapping
841 algorithm for deconvolution of fMRI data doi:10.1109/isbi48211.2021.9433821.
- 842 Uruñuela-Tremiño, E., Moia, S., Gonzalez-Castillo, J., Caballero-Gaudes, C., 2019. Deconvolution
843 of multi-echo functional MRI data with multivariate multi-echo sparse paradigm free mapping.
844 ISMRM 27th Annual Meeting and Exhibition .

- 845 Yeşilyurt, B., Uğurbil, K., Uludağ, K., 2008. Dynamics and nonlinearities of the bold response at
846 very short stimulus durations. Magnetic resonance imaging 26, 853–862. doi:10.1016/j.mri.
847 2008.01.008.
- 848 Zhang, X., Pan, W.J., Keilholz, S.D., 2020. The relationship between BOLD and neural activity
849 arises from temporally sparse events. NeuroImage 207, 116390. doi:10.1016/j.neuroimage.
850 2019.116390.
- 851 Zoeller, D., Sandini, C., Karahanoglu, F.I., Schaer, M., Eliez, S., Van De Ville, D., 2019. Large-
852 scale brain network dynamics provide a measure of psychosis and anxiety in 22q11.2 deletion
853 syndrome. Biological Psychiatry: Cognitive Neuroscience and Neuroimaging 4, 881–892. doi:10.
854 1016/j.bpsc.2019.04.004.
- 855 Zöller, D., Sandini, C., Karahanoğlu, F.I., Padula, M.C., Schaer, M., Eliez, S., Ville, D.V.D.,
856 2019. Large-scale brain network dynamics provide a measure of psychosis and anxiety in 22q11.2
857 deletion syndrome. Biological Psychiatry: Cognitive Neuroscience and Neuroimaging 4, 881–892.
858 doi:10.1101/551796.

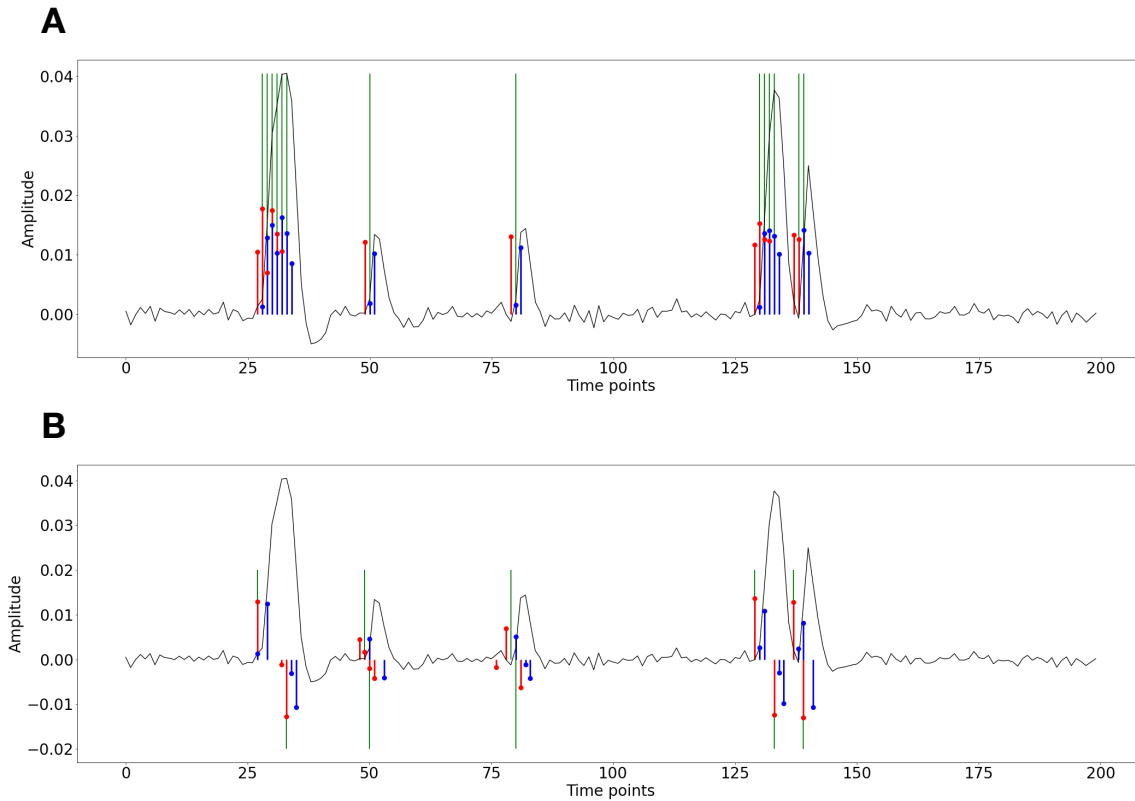


Figure S1: Activity-inducing (A) and innovation (B) signals estimated with PFM (red) and TA (blue) using their built-in HRF as opposed to using the same. The black line depicts the simulated signal, while the green lines indicate the onsets of the simulated neuronal events. X axis shows time in TRs.

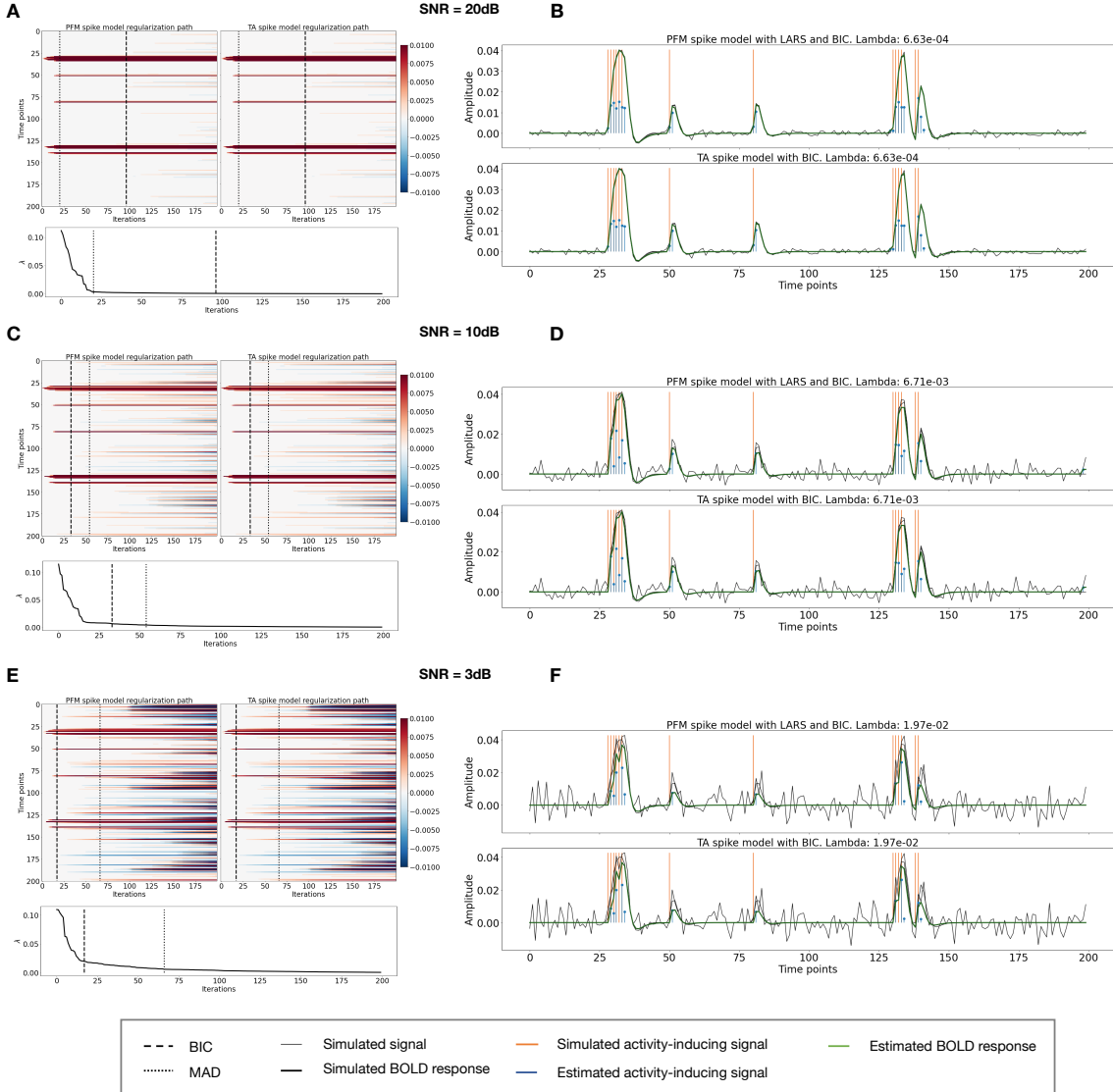


Figure S2: Spike model simulations. (Left) Heatmap of the regularization paths of the activity-inducing signal estimated with PFM and TA as a function of λ (increasing number of iterations in x-axis), whereas each row in the y-axis shows one time-point. Vertical lines denote iterations corresponding to the Akaike and Bayesian Information Criteria (AIC and BIC) optima. (Right) Estimated activity-inducing (blue) and activity-related (green) signals when set based on BIC. All estimates are identical, regardless of SNR.

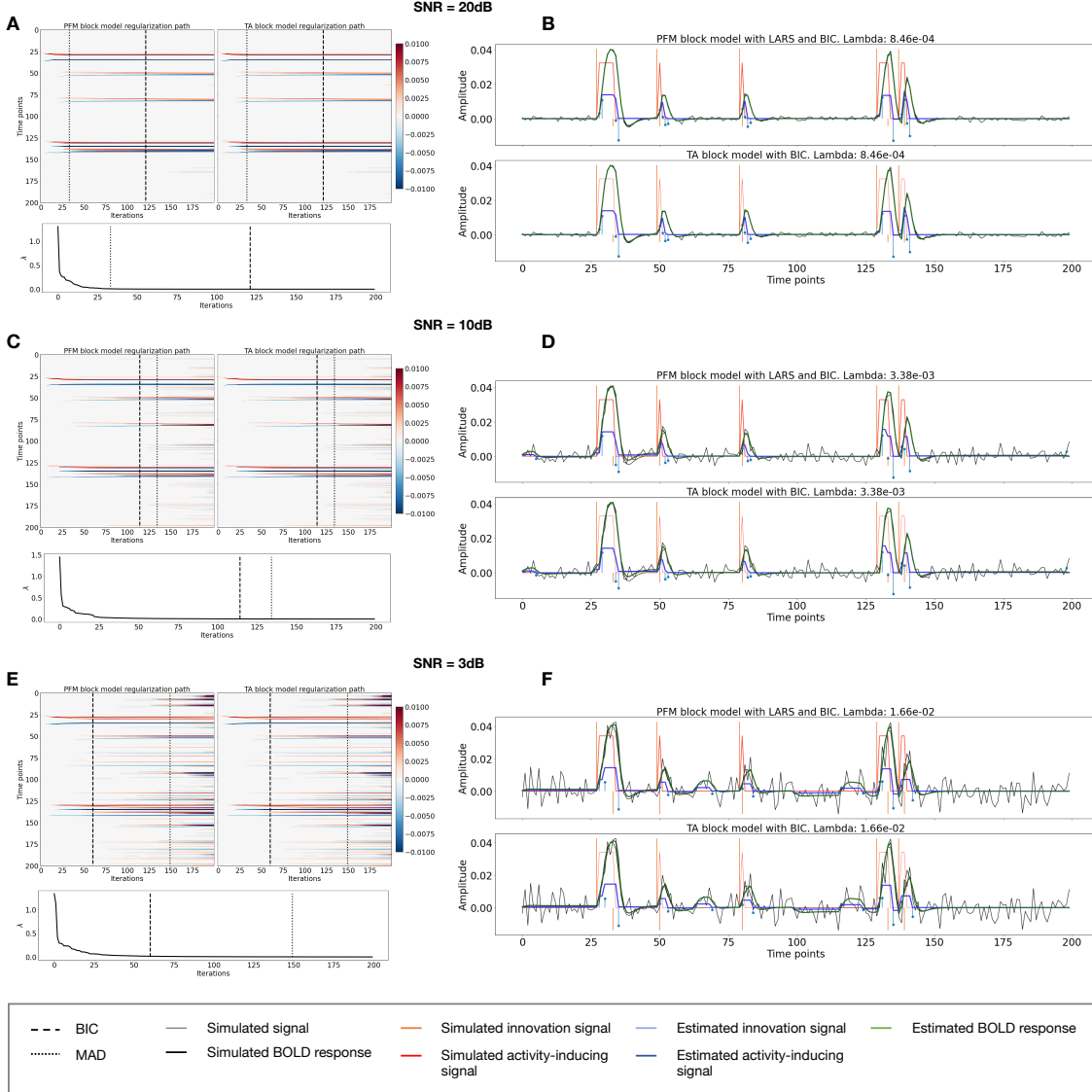


Figure S3: Block model simulations. (Left) Heatmap of the regularization paths of the innovation signal estimated with PFM and TA as a function of λ (increasing number of iterations in x-axis), whereas each row in the y-axis illustrates one time-point. Vertical lines denote iterations corresponding to the Akaike and Bayesian Information Criteria (AIC and BIC) optima. (Right) Estimated innovation (blue) and activity-related (green) signals when λ is set based on BIC. All the estimates are identical when compared between the PFM and TA cases, regardless of SNR.

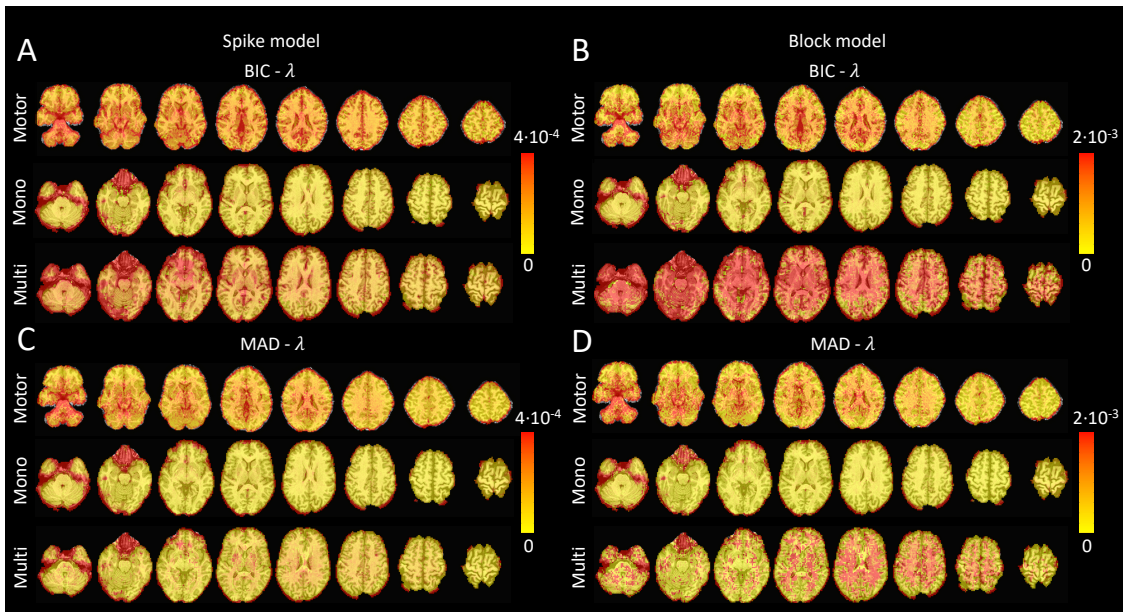


Figure S4: Values of λ across the different voxels in the brain used to estimate (A) the activity-inducing signal (spike model) and (B) the innovation signal (block model) with the BIC selection, as well as (C) the activity-inducing signal (block model) and (D) the innovation signal (block model) with a MAD-based selection. The λ maps are shown for the three experimental fMRI datasets: the motor task (Motor), the monoband resting-state (Mono), and the multiband resting-state (Multi) datasets.

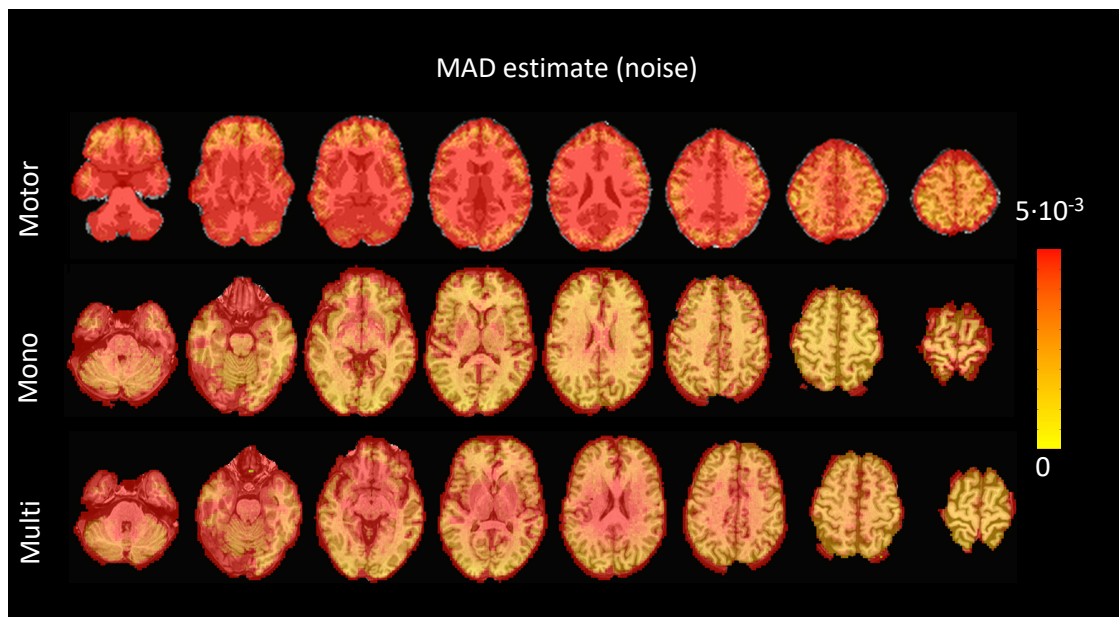


Figure S5: Values of the MAD estimate of standard deviation of the noise across the different voxels in the brain for the three experimental fMRI datasets: the motor task (Motor), the monoband resting-state (Mono), and the multiband resting-state (Multi) datasets.

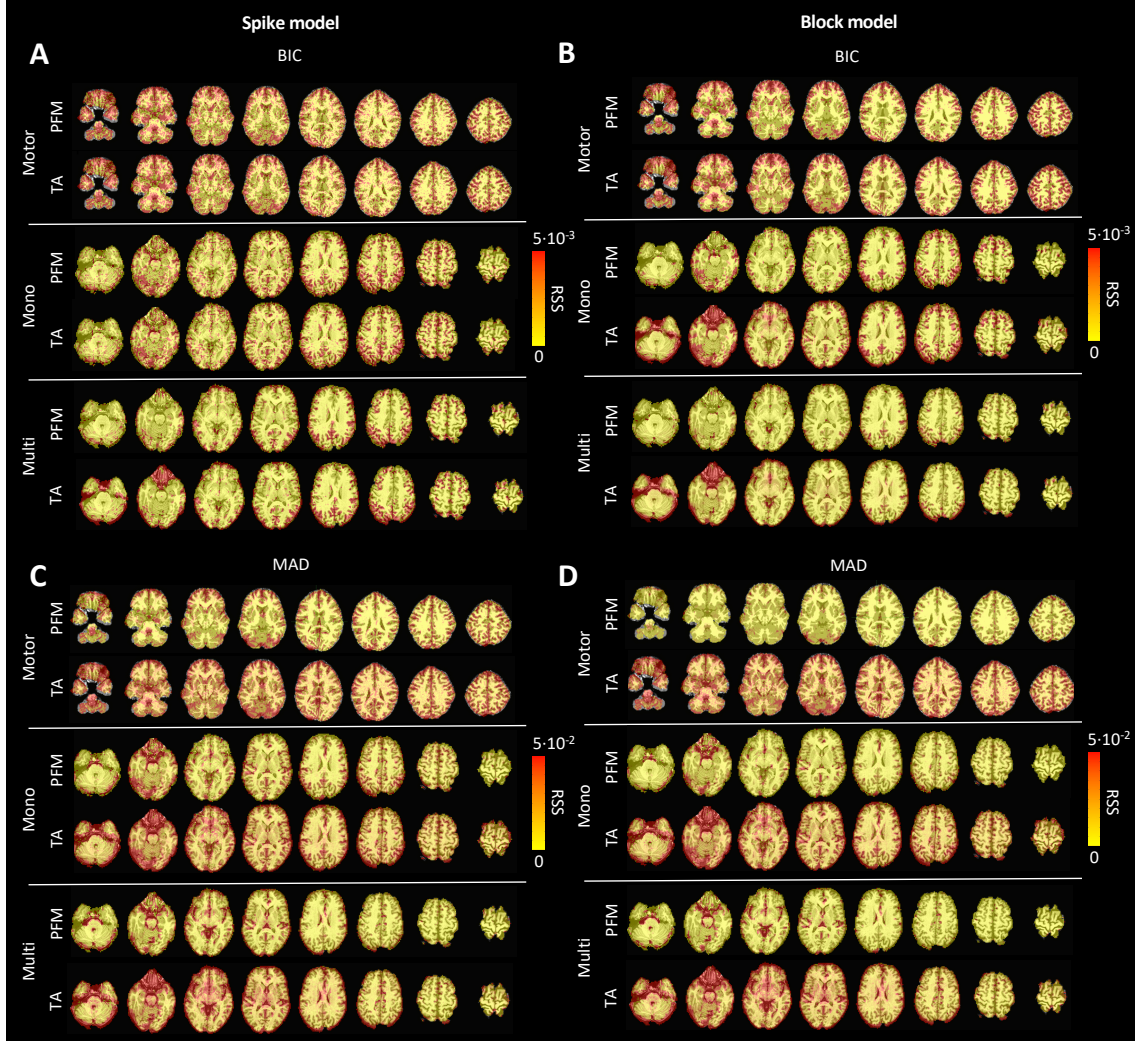


Figure S6: Root sum of squares (RSS) comparison between Paradigm Free Mapping and Total Activation for the three experimental fMRI datasets: the motor task (Motor), the monoband resting-state (Mono), and the multiband resting-state (Multi) datasets. RSS maps are shown for the spike (left) and block (right) models solved with a selection of λ based on the BIC (top) and MAD (bottom) criteria.

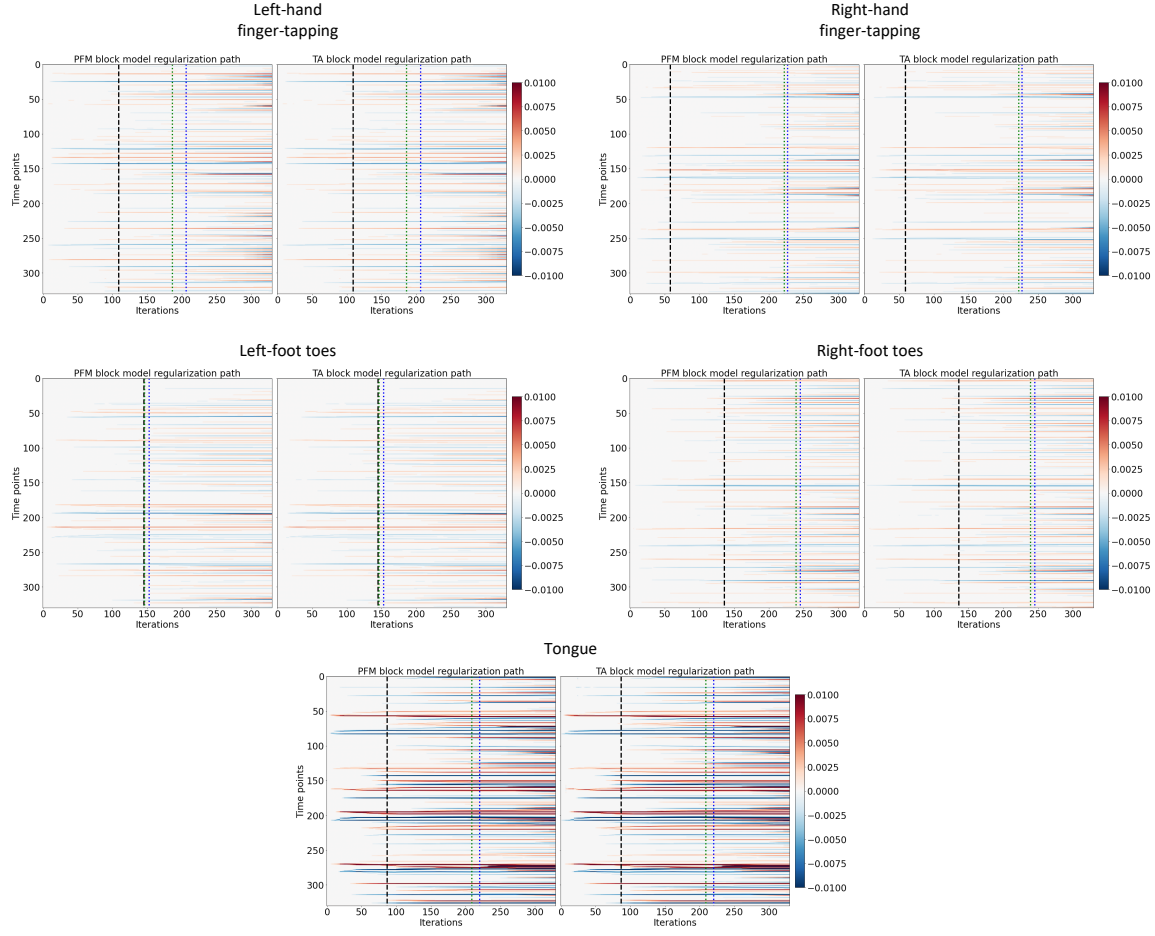


Figure S7: Regularization paths of the innovation signal estimated with PFM and TA as a function of λ (increasing number of iterations in x-axis, whereas each row in the y-axis shows one time-point) for the representative voxels of the motor task shown in Figure 5. Vertical lines denote selections of λ corresponding to the BIC (black), MAD based on LARS residuals (blue) and MAD based on FISTA residuals (green) optima.

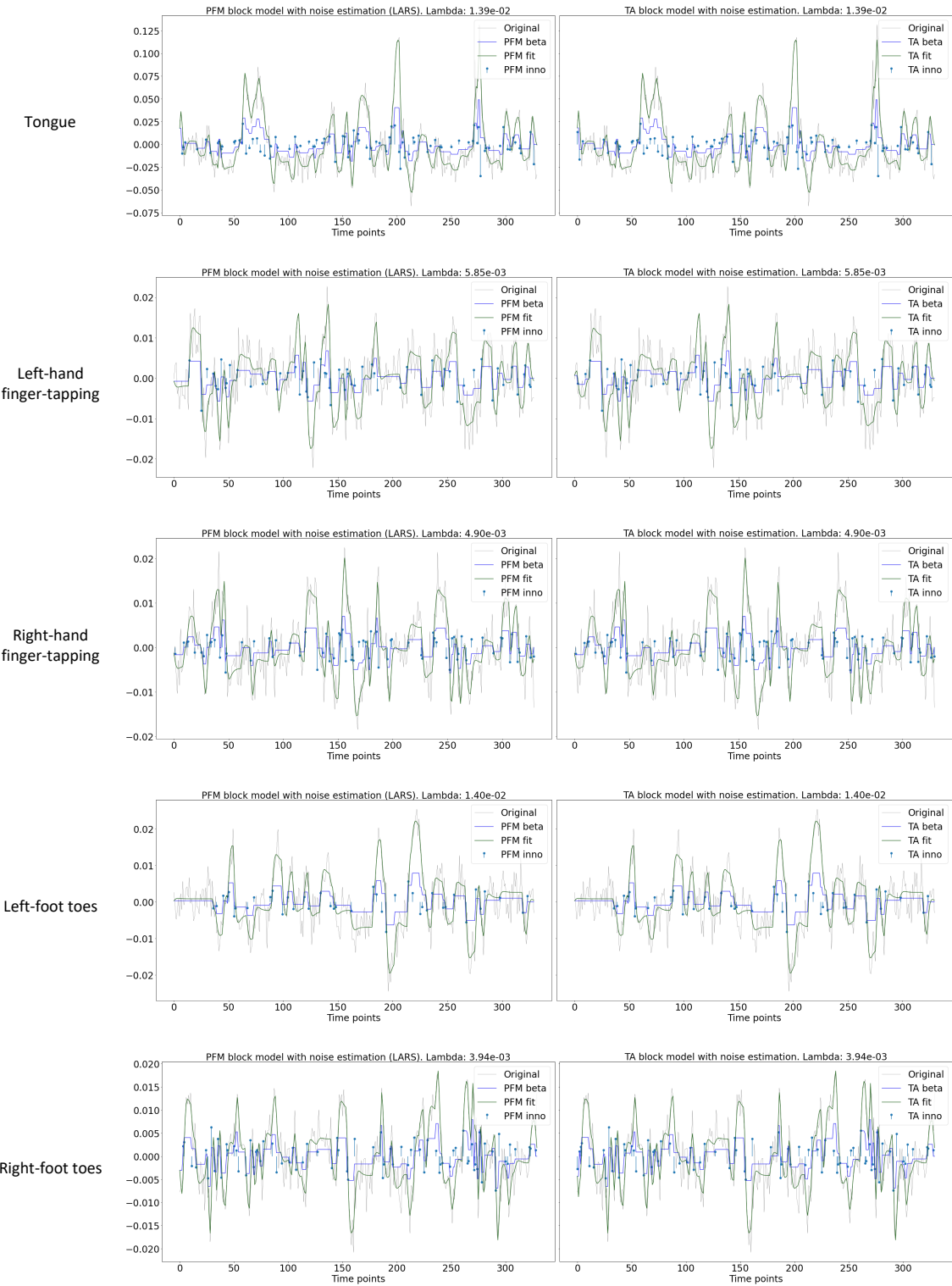


Figure S8: Estimated innovation signal (blue) and activity-related signal (green) for the representative voxels of the motor task shown in Figure 5 with the MAD selection of λ made by TA, i.e., employing the same λ with both PFM and TA.

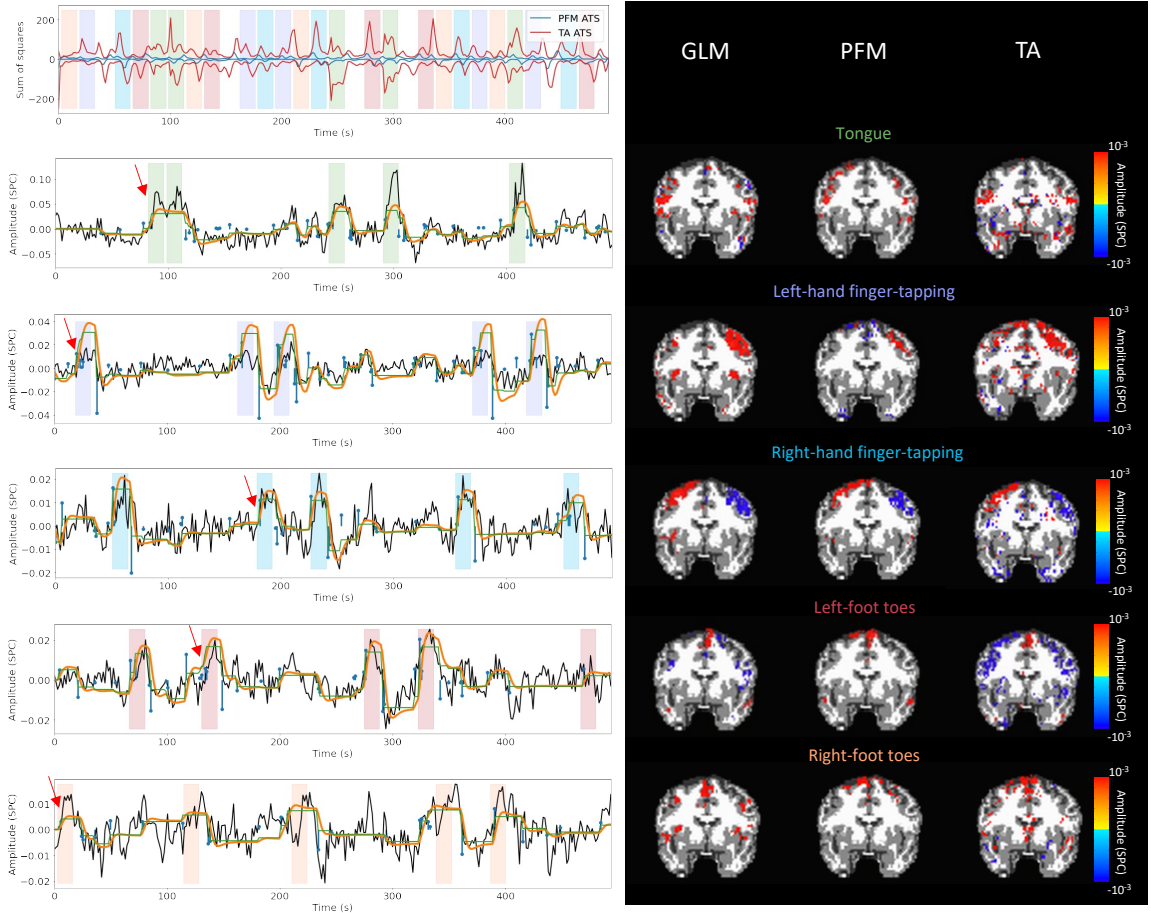


Figure S9: Activity maps of the motor task using a selection of λ based on the MAD estimate. Row 1: Activation time-series of the innovation signals estimated by PFM (in blue) or TA (in red) calculated as the sum of squares of all voxels at every timepoint. Positive-valued and negative-valued contributions were separated into two distinct time-courses. Color-bands indicate the onset and duration of each condition in the task (green: tongue, purple: left-hand finger-tapping, blue: right-hand finger-tapping, red: left-foot toes, orange: right-foot toes). Rows 2-6: time-series of a representative voxel for each task with the PFM-estimated innovation (blue), PFM-estimated activity-inducing (green), and activity-related (i.e., fitted, orange) signals, with their corresponding GLM, PFM, and TA maps on the right. The maps shown on the right are sampled at the time-point labeled with the red arrows and display the innovation signals at that moment across the whole brain.

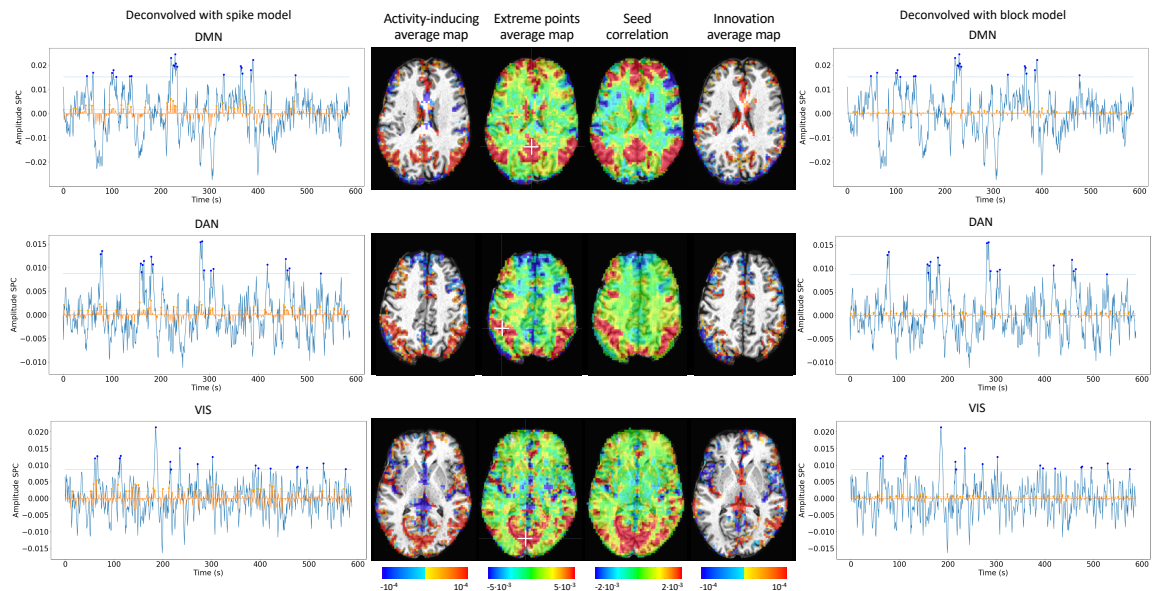


Figure S10: Activity-inducing CAPs (left) and innovation CAPs (right) obtained with the PFM-estimated activity-inducing and innovation signals respectively, using a MAD-based selection of λ . Time-points selected with a 95th percentile threshold are shown over the average time-series (blue) in the seed region (white-cross) and the deconvolved signal (orange). CAPs and seed correlation maps are illustrated in the center.